nature materials

ARTICLES

https://doi.org/10.1038/s41563-022-01287-1

Check for updates

Robust superconductivity in magic-angle multilayer graphene family

Jeong Min Park[1,3] ✉, Yuan Cao[1,3], Li-Qiao Xia[1], Shuwen Sun[1], Kenji Watanabe[2], Takashi Taniguchi[2] and Pablo Jarillo-Herrero[1] ✉

The discovery of correlated states and superconductivity in magic-angle twisted bilayer graphene (MATBG) established a new platform to explore interaction-driven and topological phenomena. However, despite multitudes of correlated phases observed in moiré systems, robust superconductivity appears the least common, found only in MATBG and more recently in magic-angle twisted trilayer graphene. Here we report the experimental realization of superconducting magic-angle twisted four-layer and five-layer graphene, hence establishing alternating twist magic-angle multilayer graphene as a robust family of moiré superconductors. This finding suggests that the flat bands shared by the members play a central role in the superconductivity. Our measurements in parallel magnetic fields, in particular the investigation of Pauli limit violation and spontaneous rotational symmetry breaking, reveal a clear distinction between the $N=2$ and $N>2$-layer structures, consistent with the difference between their orbital responses to magnetic fields. Our results expand the emergent family of moiré superconductors, providing new insight with potential implications for design of new superconducting materials platforms.

Moiré quantum matter results from stacking two or more atomically thin materials with a lattice mismatch or at a relative twist angle[1]. Motivated by the discovery of magic-angle twisted bilayer graphene (MATBG)[2,3], in the past few years moiré systems with different types of constituent layers and structures have been created, hosting a number of correlated and topological states. Phenomena including but not limited to correlated insulators, quantum anomalous Hall effect, ferromagnetism, and generalized Wigner crystals have been discovered and reproduced in various new moiré systems[4–19]. However, for the first few years robust and reproducible moiré superconductivity was seen only in MATBG[3,20,21], despite reports of signatures of superconductivity in a few other systems[5,6,8,9,11,15,22,23].

More recently, robust and highly tuneable superconductivity has been demonstrated in magic-angle twisted trilayer graphene (MATTG)[24,25]. Remarkably, the superconductivity in MATTG persists up to in-plane magnetic fields ~3 times larger than the Pauli limit for conventional BCS superconductors[26], whereas the critical magnetic field in MATBG did not substantially violate its nominal Pauli limit[3]. The similarities and differences between MATBG and MATTG raise the question of what the key ingredients needed to realize robust moiré superconductivity are, and whether the two systems may be part of a larger family of new superconductors. Practically, it would be desirable to find a reliable way to construct new moiré superconductors, as the existence of flat bands alone does not guarantee superconductivity, as demonstrated in several other graphene-based moiré systems[7–12]. Such investigations could also substantially help in understanding of the mechanism underlying these superconductors.

When two layers of monolayer graphene (MLG) are twisted at a small angle[27–29], hybridization between the Dirac bands in the graphene layers can give rise to unique flat bands where the Fermi velocity vanishes. This happens when the twist angle is close to a series of 'magic' angles. Such twisted bilayer graphene structure, with the first 'magic' angle of around 1.1°, has been intensively studied, providing insights into the nature of the correlated states, non-trivial topology and superconductivity[2,3,20,21,30–36]. It has been theoretically shown[37] that for three or more twisted layers of graphene, there are similar series of 'magic' angles if the layers are alternatively twisted by $(\theta,-\theta,\theta,\ldots)$ (Fig. 1a). The values of such angles can be analytically computed from the bilayer value in the chiral limit, where the interlayer hopping at AA sites is turned off[37]. As illustrated in Fig. 1b, they are in fact elegantly related by simple trigonometric transformations, that is the largest magic angle can be expressed as $\theta_N = \theta_\infty \cos\frac{\pi}{N+1}$, where N is the number of layers and $\theta_\infty = 2\theta_{N=2}$ is the asymptotic limit of the largest magic angle as $N\to\infty$. As N increases, the magic angle increases and the moiré length scale decreases. The real magic-angle values deviate slightly from the values in the chiral limit. Figure 1d–g shows the electronic bands corresponding to two layers to five layers calculated using a continuum model[28]. In these calculations, we used twist angles that are the same as the respective devices we measured, which are all close to the respective magic angles. Notably, all these 'magic' structures host a pair of flat bands with extremely small dispersion. MATBG, which is the first in the series, has a single pair of flat bands near zero energy that are isolated from all other dispersive bands, whereas for the structures with $N>2$ layers, there are extra bands that form $N-2$ additional Dirac points at low energies (per valley and spin). Due to the presence of these extra bands in $N>2$ layers, the electronic structures are strongly modified upon application of an out-of-plane displacement field, which tends to hybridize the flat bands with other dispersive bands (Extended Data Fig. 1).

This 'family' of magic-angle moiré structures shares a number of common properties. Regardless of the number of layers, these structures have a single moiré periodicity determined by θ, and each flat band hosts a density of $n_s = 8\theta^2/\sqrt{3}a^2$ (including valley and spin degeneracies), where $a=0.246$ nm is the lattice constant of graphene. It is therefore convenient to use $\nu = 4n/n_s, -4<\nu<4$ to describe the carrier density n within the flat bands. All members

[1]Department of Physics, Massachusetts Institute of Technology, Cambridge, MA, USA. [2]National Institute for Materials Science, Tsukuba, Japan. [3]These authors contributed equally: Jeong Min Park, Yuan Cao. ✉e-mail: parkjane@mit.edu; pjarillo@mit.edu

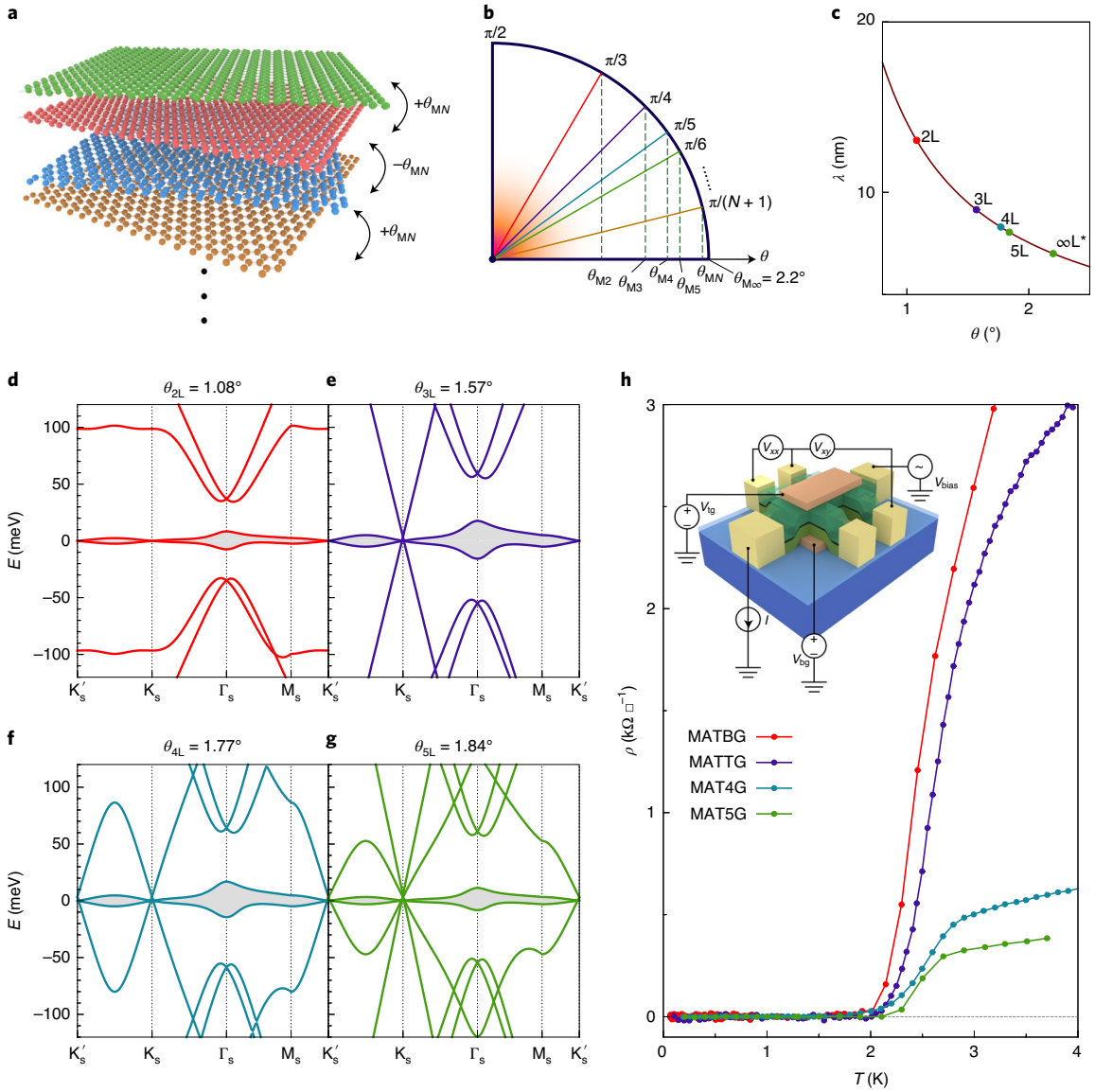

Fig. 1 | Magic-angle multilayer graphene. a, Twisted multilayer graphene with alternating twist angles θ_{MN} and $-\theta_{MN}$ between the adjacent layers, where θ_{MN} is the magic angle θ_M specific to an N-layer structure. **b**, In the chiral limit, θ_{MN} can be obtained for any N from the asymptotic value $\theta_{M\infty} = 2.2°$, by a simple trigonometric transformation. **c**, Dependence of the moiré wavelength λ on the twist angle. Note that we only consider structures with atomic alignment between the nth and $(n+2)$th layers (L), so that a single moiré wavelength can be defined[37]. **d**–**g**, Single-particle band structures for TBG (**d**), TTG (**e**), T4G (**f**) and T5G (**g**), respectively, at representative angles near their respective magic angle. The flat bands that are shared by all systems are colour-coded with grey. The flat bands in MATBG are isolated from all other dispersive bands by band insulators, whereas $N > 2$ structures have extra bands coexisting with them. The extra bands consist of either pristine Dirac-like bands or non-magic-angle-like TBG bands, depending on N. **h**, Resistivity ρ versus temperature T curves for MATBG (filling factor $\nu = -2.32$), MATTG ($\nu = -2.4$ and electric displacement field $D/\varepsilon_0 = -0.44\,\mathrm{V\,nm^{-1}}$), MAT4G ($\nu = 2.37$ and $D/\varepsilon_0 = -0.32\,\mathrm{V\,nm^{-1}}$) and MAT5G ($\nu = 3.05$ and $D/\varepsilon_0 = 0.23\,\mathrm{V\,nm^{-1}}$) ($N = 2, 3, 4, 5$), showing superconducting transitions in all four systems at their respective magic angle. Their twist angles correspond to the same values used for the calculations in 1d–g, which are indicated in 1c as well. The normal-state resistivities of MAT4G and MAT5G are smaller than MATBG and MATTG, probably due to the presence of the extra dispersive bands. Data shown for MAT4G and MAT5G are from device 4B and device 5A, respectively (see Extended Data Figs. 2–4 for the list of devices).

of the family globally retain the C_{2z} symmetry of graphene (see Methods for discussion of atomic alignment). For odd N, the atomic structure has an out-of-plane mirror symmetry M_z, whereas for even N this is replaced by a C_2 rotation axis that lies in the x–y plane. In previous works[2,3,24,25], MATBG and MATTG have both been shown to exhibit correlated insulator/resistive states at $\nu = \pm 2$, as well as superconductivity in the vicinity of these states, with critical temperatures up to ~3 K. As the flat bands in magic-angle structures with $N > 2$ can be mathematically mapped onto those in $N = 2$ (MATBG), it might be expected that these are also potential hosts of superconductivity.

We fabricated and measured high-quality magic-angle tetralayer and pentalayer graphene devices (MAT4G and MAT5G, respectively) and observed robust superconductivity in both systems, thus establishing alternating twist magic-angle multilayer graphene as a new 'family' of robust moiré superconductors. We measured multiple MAT4G and MAT5G devices (Extended Data Figs. 2–4) and, remarkably, nearly all showed robust superconductivity (Methods

and Extended Data Figs. 2, 4 and 5). Our device yield for MATTG superconducting devices is also very high, which may indicate that the superconducting phase in magic-angle systems with $N>2$ is less susceptible to relaxation than is the case for MATBG (for which about 50% of devices relax towards smaller angles and thus are not superconducting). In general, one expects moiré structures with more layers and larger twist angles to be intrinsically less susceptible to mechanical relaxation[38,39]. Figure 1h shows representative resistivity versus temperature curves for all four members of the family. These curves have been chosen for filling factors and displacement fields where the Berezinskii–Kosterlitz–Thouless transition temperature T_{BKT} was around the maximum for each device. In particular, for the new members MAT4G and MAT5G, T_{BKT} is ~2 K and ~2.2 K, respectively.

The normal-state resistivity in MAT4G and MAT5G is considerably lower than that in MATBG and MATTG, possibly due to the presence of extra highly dispersive Dirac bands, which provide parallel conducting channels. Figure 2a,b shows the ν–T phase diagrams of MAT4G and MAT5G, respectively (see Extended Data Fig. 4 for other devices). The range of filling factors in which the superconductivity appears in MAT4G and MAT5G is generally wider than in MATBG and MATTG, starting close to $\nu=\pm1$ and reaching beyond $\nu=\pm3$. In particular, superconductivity in MAT5G extends to or can even reach beyond $\nu=+4$ (Extended Data Fig. 2). Considering that MATTG also had a wider dome compared with MATBG[24,25], this observation suggests that increasing the number of layers could possibly increase the phase space robustness of the superconductivity. However, one should also note that for $N>2$, ν does not indicate the filling factor of the flat bands, because some of the carriers induced by the gates fill the dispersive bands. This effect should be more pronounced as N increases, as the number of additional dispersive Dirac bands is $N-2$. Moreover, as N increases, an inhomogeneous distribution of charge carriers among the layers could alter the effective filling factor in the flat band (Methods and Extended Data Fig. 6). In addition, the correlated resistive states at $\nu=\pm2$, if present, are less resistive than those in MATTG[24], in some cases even absent in the phase diagram (see Extended Data Fig. 2 for the full ν–D phase space for the systems), in contrast to the relatively insulating states observed in MATBG[2,20,21]. This trend again might be attributed to the presence of additional Dirac bands at the Fermi level corresponding to $\nu=\pm2$ as N increases. The presence of such bands would make the overall structure gapless even if the flat band opens a correlated gap.

To further confirm the superconductivity in the 'magic' family, we measured the voltage–current (V–I) characteristics in both MAT4G and MAT5G (Fig. 2d,e). The sharp switching behaviour in the V–I curves in all the devices (Extended Data Fig. 4) confirms the true, robust superconductivity in these new members of the family. In addition, we also performed measurements of the critical current versus perpendicular magnetic field, which reveal a Fraunhofer-like oscillation pattern (Fig. 2c, for MAT4G device). We note that due to the absence of strongly insulating states in these multilayer systems, the Fraunhofer-like pattern could only be obtained by constructing a gate-defined Josephson junction, as previously done in MATBG[40,41] (Methods and Extended Data Fig. 7). The Ginzburg–Landau coherence length measured in MAT4G is short, at around 20 nm (see Extended Data Fig. 4 for other devices and Methods for discussion), suggesting relatively strong coupling, as observed in MATTG[24]. Similar to MATTG, all of these properties are further tuneable upon application of the electric displacement field D (see Extended Data Fig. 2 for the full ν–D map). Extending the measurements to higher temperature (Fig. 2g,h), we find that the superconducting transition in these systems is relatively narrow in temperature, especially compared with MATBG, which typically exhibits very wide transitions. At higher temperatures, the resistivity does not show a strong temperature dependence, unlike the steep linear-in-temperature behaviour previously found in MATBG[42,43]. The weak linear-in-T behaviour observed might be the result of contributions stemming from both the flat bands and dispersive bands (the latter being very weakly T dependent[44]), although further theoretical work and experiments are needed to determine whether there are signatures of strange metal behaviour in these large N devices.

One way to obtain deeper insights into the underlying mechanisms and possible differences between the family members is through the response to magnetic fields applied parallel to the two-dimensional (2D) plane of the sample ($B_\parallel$). Typically, magnetic fields suppress superconductivity either by inducing vortices or by closing the gap via the Zeeman effect acting on the spin component of the Cooper pairs. The former effect is largely absent for $B_\parallel$ applied to a 2D superconductor, whereas the latter effect leads to a nominal Pauli paramagnetic limit, $B_P=(1.86\,\mathrm{T\,K^{-1}})\times T_c$, where T_c is the critical temperature for superconductivity, for conventional spin-singlet superconductors with negligible spin–orbit interactions. In MATBG, it has been shown that the critical in-plane magnetic field $B_{c\parallel}$ is not substantially larger than B_P, and superconductivity vanishes around such a field[3]. In MATTG, on the other hand, the effect of $B_\parallel$ is much weaker[26], and superconductivity can persist up to fields ~3 times larger than the nominal Pauli limit. This large discrepancy between MATBG and MATTG, which are close siblings in the family, may originate for a variety of reasons, including the role of in-plane orbital effects[45], a difference in superconducting pairing symmetry and/or different Cooper pair spin configurations. Moreover, the response of the superconducting state in MATBG under different $B_\parallel$ directions shows an interesting spontaneous breaking of rotational symmetry[46]. While the moiré lattice in MATBG possesses a sixfold rotational symmetry, $B_{c\parallel}$ shows only a two-fold symmetry (Fig. 3a), suggesting that a spontaneous nematic ordering occurs in the superconducting state. Examining these phenomena across other members of the family could thus help elucidate their underlying origin and provide information regarding the nature of the superconductivity.

Figure 3b–d shows longitudinal resistance R_{xx} as a function of the magnitude and direction of $B_\parallel$ up to 1 T, for MATTG, MAT4G and MAT5G, respectively (see Methods for sample tilt calibration details). In all three systems, the superconductor to normal-state transition does not display any visible dependence on the direction of $B_\parallel$, evidenced by the contours at different resistance values all being roughly circular (with random irregularities due to measurement noise). This is in stark contrast to MATBG (Fig. 3a), where elongated elliptical contours can be clearly seen, indicating a two-fold anisotropy of the $B_{c\parallel}$. We note that these measurements are taken near the boundary of the superconducting domes, since at optimal doping the superconducting state does not turn to a normal state even when $B_\parallel=1$ T is applied, which is the highest available field in our vector magnet for the sample mounting configuration required for measuring the angle-dependent critical field.

To obtain $B_{c\parallel}$ at base temperature, we rotated the samples so that an in-plane field up to 10 T could be applied. These high-field measurements reveal violation of the Pauli limit in both MAT4G and MAT5G, to a similar extent as in MATTG[26]. Figure 3e–g shows R_{xx} versus $B_\parallel$ and T for the hole-doped and electron-doped sides of MAT4G, and electron-doped side of MAT5G, respectively, with the constant-R_{xx} contour and their respective fit to the Ginzburg–Landau expression $T\propto 1-\alpha B_\parallel^2$, where α is a fitting parameter (see Methods for details of fitting and Extended Data Fig. 8 for additional data). Three different contours at 10%, 20% and 30% of the normal-state R_{xx} were chosen for the analysis. The zero-temperature critical field $B_{c\parallel}(0)$ obtained by extrapolating the fit shows values that consistently exceed the Pauli limit by a factor of ~2 in all samples that we measured, as well as across all the superconducting domes, as shown in Fig. 3h,i. Such consistency suggests that the Pauli limit violation is probably inherent to the

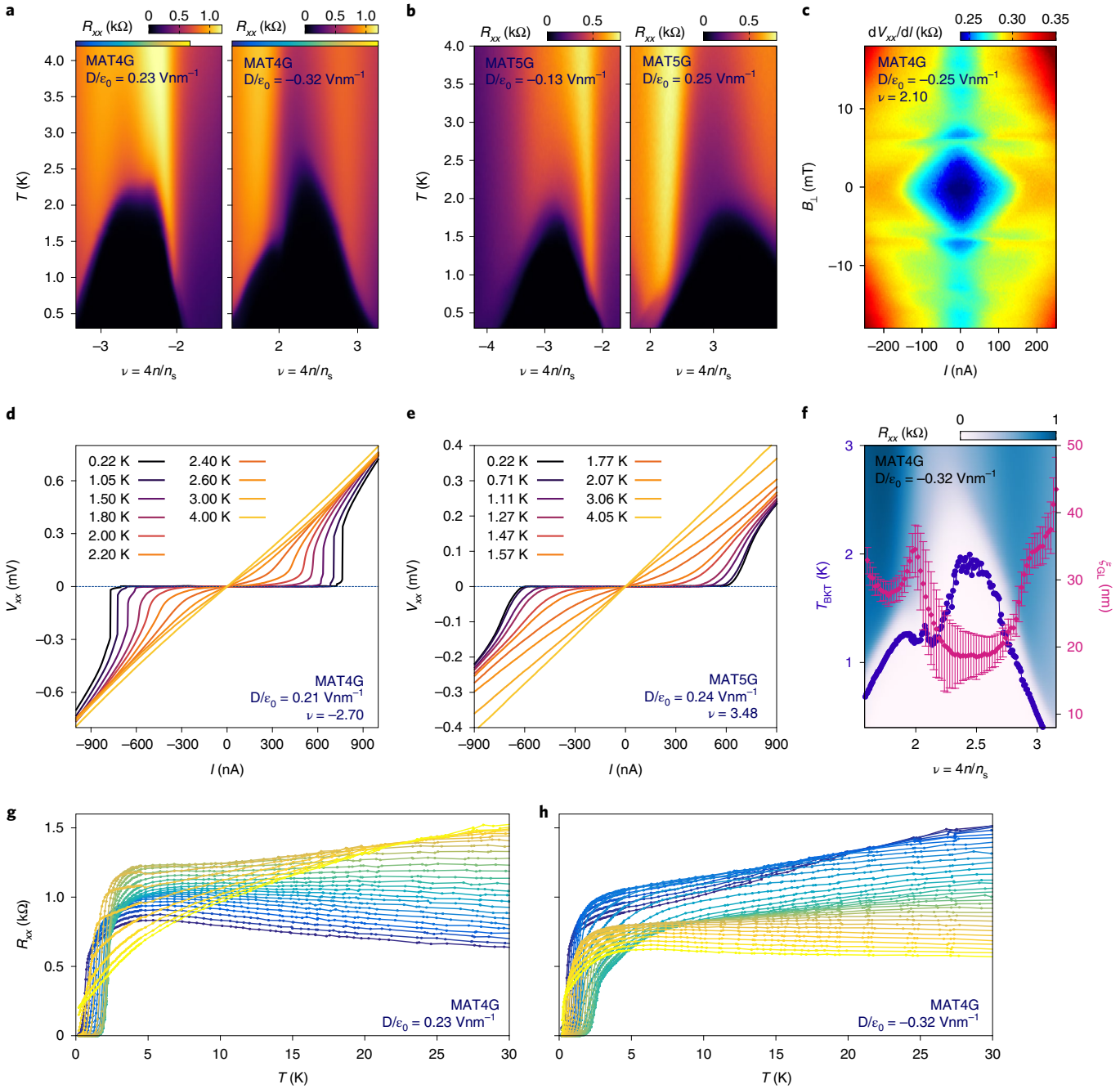

Fig. 2 | Robust superconductivity in MAT4G and MAT5G. Data are shown for device 4B and device 5B, respectively. **a**,**b**, Resistance R_{xx} versus moiré filling factor ν and temperature T for MAT4G and MAT5G, respectively. The superconducting domes span a wide density range across the flat bands. Note that in MATTG, MAT4G and MAT5G, ν includes the filling of both the flat bands and the extra dispersive bands. **c**, Differential resistance dV_{xx}/dI versus d.c. bias current I and small perpendicular magnetic field $B_\perp$, showing Fraunhofer-like oscillations in $B_\perp$. The data are measured in a split top gate geometry where the middle non-gated region is tuned to a resistive state (N) while maintaining the superconductivity of the gated regions (S), thus forming an SNS Josephson junction[40,41]. The junction is across the device 4A and 4B (Extended Data Fig. 7). **d**, Voltage (V) versus current (I) curves at T ranging from 220 mK to 4 K at $\nu = -2.70$ and $D/\varepsilon_0 = 0.21$ V nm^{-1} in MAT4G. **e**, Same measurement in MAT5G at $\nu = 3.48$ and $D/\varepsilon_0 = 0.24$ V nm^{-1}. **f**, Ginzburg–Landau coherence length ξ_{GL} versus ν at $D/\varepsilon_0 = -0.32$ V nm^{-1} in MAT4G, along with the extracted Berezinskii–Kosterlitz–Thouless transition temperature T_{BKT}. They are overlaid on a colour map of R_{xx} versus ν and T. ξ_{GL} reaches low values around 20 nm near optimal doping $\nu \approx 2.5$. The extraction is performed with 25%, 30% and 35% of normal-state resistance for the upper uncertainty bound, data point, and lower uncertainty bound, respectively (Methods). **g**,**h**, R_{xx} versus T curves in MAT4G at $D/\varepsilon_0 = 0.23$ V nm^{-1} (**g**) and $D/\varepsilon_0 = -0.32$ V nm^{-1} (**h**) across ν up to $T = 30$ K showing sharp superconducting transitions. The colour scale for the curves matches the scale bar shown in the hole-doped ($-3.33 < \nu < -1.8$) and electron-doped ($1.4 < \nu < 3.27$) plots at the top in **a**, respectively.

superconducting state in MATTG, MAT4G and MAT5G, rather than the result of spin–orbit coupling or strong coupling effects (see ref. [26] for a discussion of these effects).

Our experiments clearly establish that, while all members of the magic-angle graphene family show similarities that are likely to originate from their respective flat band physics, such as the range

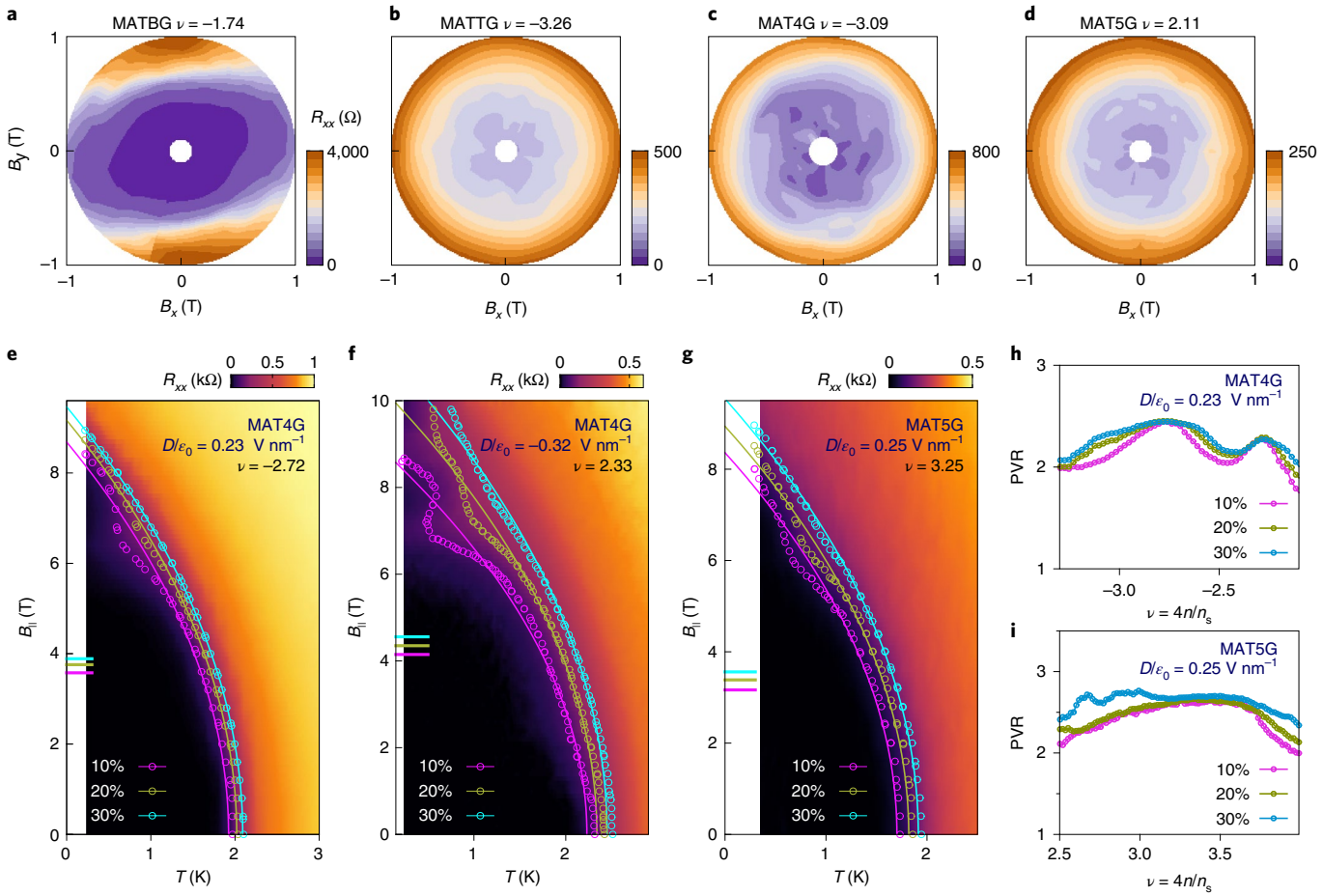

Fig. 3 | In-plane magnetic field dependence of the superconducting states. a–d, Polar maps of the in-plane magnetic field response of R_{xx} in MATBG, MATTG, MAT4G (device 4C) and MAT5G (device 5B), at $\nu = -1.74$ and $T = 0.07$ K (**a**), $\nu = -3.26$ and $T = 0.1$ K (**b**), $\nu = -3.09$ and $T = 0.2$ K (**c**) and $\nu = 2.11$ and $T = 0.2$ K (**d**). MATBG shows an anisotropic response with two-fold symmetry in its in-plane critical field, while the other three systems do not show any anisotropy. **e–g**, $B_{\parallel}$–T phase diagram at $(\nu, D/\varepsilon_0) = (-2.72, 0.23\ \mathrm{V\,nm^{-1}})$ (**e**) and $(2.33, -0.32\ \mathrm{V\,nm^{-1}})$ (**f**) in MAT4G (device 4B), and $(3.25, 0.25\ \mathrm{V\,nm^{-1}})$ in MAT5G (device 5B) (**g**). The data points denote constant-resistance contours at 10%, 20% and 30% of the zero-field normal-state resistance. Solid curves are fit to the Ginzburg–Landau expression $T \propto 1 - \alpha B_{\parallel}^2$ (α is a fitting parameter). We find the critical magnetic fields $B_{c\parallel}(0)$ by extrapolating the contours to zero temperature. The coloured ticks on the $B_{\parallel}$ axis represent the corresponding nominal Pauli limit for each threshold. We note that in **e** and **f** there are some hints of re-entrant superconducting behaviour at high field[26]. **h**,**i**, Pauli violation ratio (PVR), the ratio between $B_{c\parallel}(0)$ and the nominal Pauli limit, across ν in MAT4G (device 4B, **h**) and MAT5G (device 5B, **i**). In both systems, PVR is around 2–3.

of density where superconductivity is strongest, the in-plane magnetic field response sharply distinguishes $N = 2$ (that is MATBG) from family members with $N > 2$. This is surprising, as from a symmetry point of view, members with even N share the same in-plane C_2 rotation symmetry and members with odd N share the same mirror symmetry M_z. One would thus expect that systems with even layers and odd layers behave similarly within their respective groups, while distinct across them. These observations do not depend substantially on the presence or absence of a displacement field (Methods and Extended Data Fig. 9), and are therefore necessarily intrinsic to their respective flat bands, even though all of these can be mapped to the MATBG ones[37].

Here we attempt to give a possible unified explanation of these experimental findings by considering orbital effects in an in-plane magnetic field. Both the strong violation of the nominal Pauli limit and the absence of nematicity in the magic-angle structures with $N > 2$ layers could be accounted for by a reduced in-plane orbital effect as a result of symmetry. In 2D superconductors such as the magic-angle family, while $B_{\parallel}$ does not induce vortices, the effective momentum boost experienced when electrons tunnel between different layers (proportional to $B_{\parallel}$ and the interlayer distance) can distort the shape of the Fermi surface, and this can act as a pair-breaking effect for superconductivity. This was considered for MATBG[45,46] and the pair-breaking effect has a similar magnitude to that resulting from spin Zeeman effect, with an effective g-factor around 2. In other words, the in-plane orbital effect in MATBG could account for the suppression of superconductivity at fields of the order of the nominal Pauli limit.

When more layers are added, however, the in-plane orbital effects between layers tend to cancel each other out, rather than being additive. This is conceptually sketched in Fig. 4a. If we consider any internal layer in the stack, for example a layer twisted at $-\theta/2$, the electrons that tunnel from the layers above it and below it (both of which are at angle $\theta/2$) would experience opposite momentum boost. From a perturbation theory point of view, the first-order effect on the spectrum, proportional to $B_{\parallel}$, would be partially or fully cancelled depending on N (see Methods for full derivation). In Fig. 4b, we calculated the mean orbital g-factor, g_{orb}, in the flat bands of magic-angle structures with $N = 2, 3, 4, 5, 6$, in the absence and presence of a displacement field (Methods; note that a similar calculation and interpretation was recently made independently in a theoretical work[47]). To interpret the role of g_{orb}, a system with $g_{\mathrm{orb}} = 2$

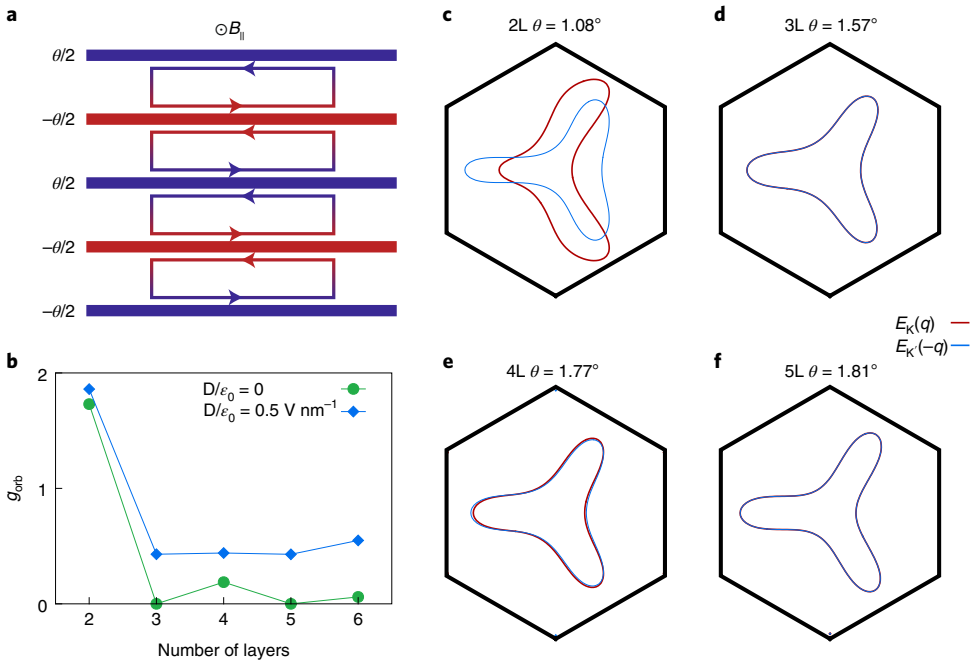

Fig. 4 | In-plane magnetic field orbital effect. a, Schematic showing cancellation of the orbital effect under $B_{\parallel}$ in the alternating twist structures. Solid blue and red lines represent graphene layers with alternating twist angles, and the arrowed loops show that the direction of the momentum boost for hopping between adjacent pairs of layers is opposite. For the internal layers in $N>2$ structures, this results in a greatly reduced in-plane orbital effect (see Methods for mathematical derivation). **b**, Calculated orbital *g*-factor, g_{orb}, for *N*-layer MATNG. Both at zero and finite *D*, MATBG has the highest coupling to the in-plane field, whereas systems with $N>2$ have much smaller g_{orb}. Finite *D* breaks M_z and leads to increased g_{orb} compared with the case of $D=0$. **c**–**f**, Calculated Fermi contours at K and K′ valleys of MATBG (**c**), MATTG (**d**), MAT4G (**e**) and MAT5G (**f**) near their magic angles under $B_{\parallel}$. The magnetic field is along the horizontal direction and the magnitude is set to 20 T to exaggerate the effect. The Fermi surface is distorted differently for K and K′ valleys. For MATBG, this leads to a considerable orbital pair-breaking effect, whereas for $N>2$ structures such distortion is minimal.

would have its critical field at the Pauli limit and $g_{orb}<2$ would lead to Pauli limit violation. MATBG has a $g_{orb}\lesssim 2$. For odd *N*, the mirror symmetry (M_z) of the system prohibits the in-plane magnetic fields from coupling to the system[45,48], and g_{orb} is strictly zero in the absence of a displacement field. For even $N\geq 4$, although a finite value of g_{orb} is allowed by symmetry, our calculations show that g_{orb} is greatly suppressed compared with MATBG. Therefore, the trend of g_{orb} with *N* qualitatively explains why all $N>2$ structures violate the Pauli limit while $N=2$ does not. When a displacement field is turned on, we find that the difference between even/odd *N* diminishes, but the orbital *g*-factors for all $N>2$ structures are still considerably smaller than that in MATBG. We note that as *N* increases, the distribution of the displacement field becomes highly non-uniform across the stack due to electrostatic screening from outer layers, and we have taken a simple approximation to account for such effect (Methods and Extended Data Figs. 1 and 6).

Such differences in the orbital coupling might also determine the appearance of nematicity throughout the family. Figure 4c–f shows the calculated Fermi surfaces of K and K′ valleys upon application of $B_{\parallel}$. The momentum boosts induced by $B_{\parallel}$ are opposite for K and K′ valleys. For $N=2$ (MATBG), this results in sizeable distortion of the Fermi surface, which provides a means for $B_{\parallel}$ to couple to the superconducting order parameter, and this coupling is dependent on the direction of $B_{\parallel}$. This could lead to the observed two-fold nematicity when further pinning from strain or other many-body effects such as density waves is considered[46]. In contrast, for the $N>2$ structures, the Fermi surfaces in the two valleys have minimal distortion (without a displacement field), and thus there is no direct coupling between $B_{\parallel}$ and the orbital part of the superconducting order parameter. While $B_{\parallel}$ could still couple to the spin degree of freedom, weak spin–orbit interaction in these graphene systems prevents coupling to the orbital part, and hence no nematicity or other types of anisotropic phases are likely to develop.

In the above discussions the role of electron spins was deliberately neglected, but we can consider this now. For $N>3$, the Cooper pairs clearly cannot be spin-singlets, or the Zeeman effect would suppress superconductivity at the Pauli limit. Since the superconducting states are otherwise similar across the family, there is a possibility that even MATBG is a non-spin-singlet superconductor, and the apparent conformance to the Pauli limit could be a result of the orbital effect as discussed above, with similar g_{orb} to that of the spin Zeeman effect. Similar considerations were proposed in a recent theoretical work[45].

We note that although this mechanism can qualitatively capture the effect of in-plane magnetic fields on the magic-angle superconductor family, there are still remaining puzzles. While the g_{orb} for odd *N* are expected to be zero and the critical magnetic field should be infinitely large in principle, experimentally we find Pauli limit violations of ~3 in MATTG and ~2 in MAT5G. Furthermore, the theoretically calculated g_{orb} strongly depends on the applied displacement field, whereas the measured Pauli limit violation has only minor variations with the displacement field. For $N\geq 3$, the distribution of the displacement field among the layers could be intertwined with the correlation effects in the system, and a spontaneous internal displacement field could exist in principle even when no external displacement field is applied. Slight discrepancies among the twist angles between the layers could introduce further corrections to the displacement field effects. Numerically accounting for these aspects in our calculation is beyond the scope of this work and we hope that these issues will be clarified by future research.

The discovery of superconductivity in all members of the magic-angle family from $N=2$ to $N=5$ has profound implications

on its mechanism. The presence of superconductivity regardless of the number of layers implies that the peculiar flat band that all these systems share is likely to play a crucial role in forming robust superconductivity. Moreover, the $C_{2z}T$ symmetry that all these structures share could also be an important ingredient behind the robustness of the superconductivity, as most moiré systems studied so far lacking such symmetry do not seem to be robust superconductors. These findings put strong constraints on the theories for the possible underlying mechanisms for the unusually strong superconductivity in this moiré family.

Online content

Any methods, additional references, Nature Research reporting summaries, source data, extended data, supplementary information, acknowledgements, peer review information; details of author contributions and competing interests; and statements of data and code availability are available at https://doi.org/10.1038/s41563-022-01287-1.

Received: 24 December 2021; Accepted: 10 May 2022;
Published online: 7 July 2022

References

1. Andrei, E. Y. et al. The marvels of moiré materials. *Nat. Rev. Mater.* **6**, 201–206 (2021).
2. Cao, Y. et al. Correlated insulator behaviour at half-filling in magic-angle graphene superlattices. *Nature* **556**, 80–84 (2018).
3. Cao, Y. et al. Unconventional superconductivity in magic-angle graphene superlattices. *Nature* **556**, 43–50 (2018).
4. Chen, G. et al. Evidence of a gate-tunable Mott insulator in a trilayer graphene moiré superlattice. *Nat. Phys.* **15**, 237 (2019).
5. Burg, G. W. et al. Correlated insulating states in twisted double bilayer graphene. *Phys. Rev. Lett.* **123**, 197702 (2019).
6. Shen, C. et al. Correlated states in twisted double bilayer graphene. *Nat. Phys.* **16**, 520–525 (2020).
7. Cao, Y. et al. Tunable correlated states and spin-polarized phases in twisted bilayer-bilayer graphene. *Nature* **583**, 215–220 (2020).
8. Liu, X. et al. Tunable spin-polarized correlated states in twisted double bilayer graphene. *Nature* **583**, 221–225 (2020).
9. He, M. et al. Symmetry breaking in twisted double bilayer graphene. *Nat. Phys.* **17**, 26–30 (2020).
10. Polshyn, H. et al. Electrical switching of magnetic order in an orbital Chern insulator. *Nature* **588**, 66–70 (2020).
11. Xu, S. et al. Tunable van Hove singularities and correlated states in twisted monolayer-bilayer graphene. *Nat. Phys.* **17**, 619–626 (2021).
12. Chen, S. et al. Electrically tunable correlated and topological states in twisted monolayer–bilayer graphene. *Nat. Phys.* **17**, 374–380 (2021).
13. Regan, E. C. et al. Mott and generalized Wigner crystal states in WSe_2/WS_2 moiré superlattices. *Nature* **579**, 359–363 (2020).
14. Tang, Y. et al. Simulation of Hubbard model physics in WSe_2/WS_2 moiré superlattices. *Nature* **579**, 353–358 (2020).
15. Wang, L. et al. Correlated electronic phases in twisted bilayer transition metal dichalcogenides. *Nat. Mater.* **19**, 861–866 (2020).
16. Xu, Y. et al. Correlated insulating states at fractional fillings of moiré superlattices. *Nature* **587**, 214–218 (2020).
17. Jin, C. et al. Stripe phases in WSe_2/WS_2 moiré superlattices. *Nat. Mater.* **20**, 940–944 (2021).
18. Li, T. et al. Continuous Mott transition in semiconductor moiré superlattices. *Nature* **597**, 350–354 (2021).
19. Li, T. et al. Quantum anomalous Hall effect from intertwined moiré bands. *Nature* **600**, 641–646 (2021).
20. Yankowitz, M. et al. Tuning superconductivity in twisted bilayer graphene. *Science* **363**, 1059–1064 (2019).
21. Lu, X. et al. Superconductors, orbital magnets and correlated states in magic-angle bilayer graphene. *Nature* **574**, 653–657 (2019).
22. Chen, G. et al. Signatures of tunable superconductivity in a trilayer graphene moiré superlattice. *Nature* **572**, 215–219 (2019).
23. Zhang, X. et al. Correlated insulating states and transport signature of superconductivity in twisted trilayer graphene superlattices. *Phys. Rev. Lett.* **127**, 166802 (2021).
24. Park, J. M., Cao, Y., Watanabe, K., Taniguchi, T. & Jarillo-Herrero, P. Tunable strongly coupled superconductivity in magic-angle twisted trilayer graphene. *Nature* **590**, 249–255 (2021).
25. Hao, Z. et al. Electric field-tunable superconductivity in alternating-twist magic-angle trilayer graphene. *Science* **371**, 1133–1138 (2021).
26. Cao, Y., Park, J. M., Watanabe, K., Taniguchi, T. & Jarillo-Herrero, P. Pauli-limit violation and re-entrant superconductivity in moiré graphene. *Nature* **595**, 526–531 (2021).
27. Suárez Morell, E., Correa, J. D., Vargas, P., Pacheco, M. & Barticevic, Z. Flat bands in slightly twisted bilayer graphene: tight-binding calculations. *Phys. Rev. B* **82**, 121407 (2010).
28. Bistritzer, R. & MacDonald, A. H. Moiré bands in twisted double-layer graphene. *Proc. Natl Acad. Sci. USA* **108**, 12233–12237 (2011).
29. Lopes dos Santos, J. M. B., Peres, N. M. R. & Castro Neto, A. H. Continuum model of the twisted graphene bilayer. *Phys. Rev. B* **86**, 155449 (2012).
30. Xie, Y. et al. Spectroscopic signatures of many-body correlations in magic-angle twisted bilayer graphene. *Nature* **572**, 101–105 (2019).
31. Wong, D. et al. Cascade of electronic transitions in magic-angle twisted bilayer graphene. *Nature* **582**, 198–202 (2020).
32. Zondiner, U. et al. Cascade of phase transitions and Dirac revivals in magic-angle graphene. *Nature* **582**, 203–208 (2020).
33. Park, J. M., Cao, Y., Watanabe, K., Taniguchi, T. & Jarillo-Herrero, P. Flavour Hund's coupling, Chern gaps and charge diffusivity in moiré graphene. *Nature* **592**, 43–48 (2021).
34. Oh, M. et al. Evidence for unconventional superconductivity in twisted bilayer graphene. *Nature* **600**, 240–245 (2021).
35. Pierce, A. T. et al. Unconventional sequence of correlated Chern insulators in magic-angle twisted bilayer graphene. *Nat. Phys.* **17**, 1210–1215 (2021).
36. Xie, Y. et al. Fractional Chern insulators in magic-angle twisted bilayer graphene. *Nature* **600**, 439–443 (2021).
37. Khalaf, E., Kruchkov, A. J., Tarnopolsky, G. & Vishwanath, A. Magic angle hierarchy in twisted graphene multilayers. *Phys. Rev. B* **100**, 085109 (2019).
38. Nam, N. N. T. & Koshino, M. Lattice relaxation and energy band modulation in twisted bilayer graphene. *Phys. Rev. B* **96**, 075311 (2017).
39. Turkel, S. et al. Orderly disorder in magic-angle twisted trilayer graphene. *Science* **376**, 193–199 (2022).
40. Rodan-Legrain, D. et al. Highly tunable junctions and non-local Josephson effect in magic-angle graphene tunnelling devices. *Nat. Nanotechnol.* **116**, 769–775 (2021).
41. de Vries, F. K. et al. Gate-defined Josephson junctions in magic-angle twisted bilayer graphene. *Nat. Nanotechnol.* **16**, 760–763 (2021).
42. Cao, Y. et al. Strange metal in magic-angle graphene with near Planckian dissipation. *Phys. Rev. Lett.* **124**, 076801 (2020).
43. Polshyn, H. et al. Large linear-in-temperature resistivity in twisted bilayer graphene. *Nat. Phys.* **15**, 1011–1016 (2019).
44. Dean, C. R. et al. Boron nitride substrates for high-quality graphene electronics. *Nat. Nanotechnol.* **5**, 722–726 (2010).
45. Qin, W. & MacDonald, A. H. In-plane critical magnetic fields in magic-angle twisted trilayer graphene. *Phys. Rev. Lett.***127**, 097001 (2021).
46. Cao, Y. et al. Nematicity and competing orders in superconducting magic-angle graphene. *Science* **372**, 264–271 (2021).
47. Ledwith, P. J. et al. TB or not TB? Contrasting properties of twisted bilayer graphene and the alternating twist η-layer structures (η=3, 4, 5, …). Preprint at https://arxiv.org/abs/2111.11060 (2021).
48. Lake, E. & Senthil, T. Reentrant superconductivity through a quantum Lifshitz transition in twisted trilayer graphene. *Phys. Rev. B* **104**, 174505 (2021).

Methods

Sample fabrication. We fabricated all MATNG devices using the 'cut & stack' method described in detail in our previous work[33]. We first exfoliated single-crystal hBN (30–80 nm thick) and monolayer graphene flakes on silicon substrates (with 285 nm dry oxide), which were screened with optical microscopy for contaminations and defects. A large graphene flake was laser-cut, with a ~1 μm beam diameter, into N (= 4, 5) adjacent pieces, each 10–20 μm in size. We then used the standard dry transfer technique with poly(bisphenol A carbonate)/polydimethylsiloxane to pick up the top hBN flake and subsequently N graphene flakes, alternatively rotated by θ and $-\theta$. The stack was eventually released on a bottom hBN flake, which had been pre-transferred onto a Pd–Au alloy bottom gate and heat annealed in forming gas at 300 °C. The Hall-bar geometry was defined with electron beam lithography and reactive ion etching. Top gate and electrical contacts were made from thermally evaporated chromium and gold.

In total we fabricated and measured four MAT4G and six MAT5G devices (referring to samples with working electrical contacts and gates). Among them, three of the MAT4G devices and all six MAT5G devices showed robust superconductivity. Extended Data Figure 2 shows the ν–D phase diagram of MAT4G devices 4A, 4B and 4C and MAT5G devices 5A, 5B, 5C, 5D and 5E, which we have thoroughly measured. Previously, we fabricated and measured four MATTG devices, which all exhibited robust superconductivity. In contrast, MATBG devices undergo twist angle relaxation during fabrication much more frequently, which gives a total yield of roughly 50% at best. This difference might indicate that MATNG structures with $N > 2$ are much more robust against relaxation and/or have more robust parameter-space superconducting phase space.

Measurement setup. Transport data in MATNG were measured in a dilution refrigerator equipped with a triple-axis vector-type magnet. All sample wires have multistage low-pass filters. Current through the sample and the four-probe voltage were first amplified by 1×10^7 V A^{-1} and 1,000, respectively, using Ithaco current and voltage pre-amplifiers, and then measured with Stanford Research SR830 or SR860 lock-in amplifiers. The lock-in frequency is typically between 10 Hz and 20 Hz. We used current excitation of ~1–5 nA for resistance measurements. For d.c. bias measurements, we used a BabyDAC passing through a 10 MΩ resistor to provide the d.c. bias current, and measured the d.c. voltage with a Keysight 34461A digital multimeter connected to the voltage pre-amplifier.

In the temperature-dependent colour maps (Figs. 2a,b and 3e–g and Extended Data Figs. 4d–i, 8e,f, 9b and 9d), since the raw data were taken at non-regular intervals in temperature, we first interpolated the data into a regular grid in T before plotting. We checked that no artefacts were introduced by this interpolation.

Analysis of Ginzburg–Landau coherence length. The Ginzburg–Landau coherence length in MAT4G and MAT5G was extracted from the $B_\perp$dependence of the critical temperature T_c. We first extracted the mean-field T_c at zero $B_\perp$ by fitting the high-temperature part of the data to a straight line $r(T) = AT + B$, and then found the intersection of $R_{xx}(T)$ with $p \times r(T)$, where p is the percentage of normal resistance. The Ginzburg–Landau coherence length ξ_{GL} was then obtained from linear fitting of T_c against $B_\perp$, and the x intercept is equal to $\Phi_0/(2\pi\xi_{GL}^2)$, where $\Phi_0 = h/2e$ is the superconducting flux quantum. The different thresholds yielded slightly different but consistent coherence lengths, which we plotted in Fig. 2f as the data points (30%) and error bars (25%, 35%). This procedure is the same as performed in our previous work (ref. [24]).

Field calibration. Since measurements of both Pauli limit violation and rotational symmetry breaking were performed in a triple-axis magnet, careful calibration was necessary to make sure that any magnetic field component perpendicular to the sample due to sample tilt is compensated. For Pauli limit violation measurements, the sample was mounted parallel to the z axis and we used the z-axis magnet to apply large magnetic fields up to 10 T, while using the x-axis magnet to compensate for any sample tilt. For rotational symmetry breaking measurements, we mounted the sample parallel to the x–y plane and applied magnetic fields up to a magnitude of 1 T along any direction in this plane, while using the z-axis magnet to apply the compensation field.

In both cases, we used the MATNG sample itself as a sensitive field sensor, because the resistance R_{xx} is very sensitive to $B_\perp$ when it is doped near the edge of the superconducting dome. Detailed calibration methods were published in previous works[26,46]. For the Pauli limit violation measurements, the residual $B_\perp$ after the calibration procedure is typically less than ±5 mT when $B_\parallel = 10$ T is applied. For the rotational symmetry breaking measurements, the residual $B_\perp$ is typically less than 2 mT when $B_\parallel = 1$ T is applied. These residual fields are small enough that they do not have any appreciable effect on the measured data.

Analysis of Pauli violation ratio. To extract the Pauli violation ratio (PVR), we first extracted the normal-state resistance similar to the coherence length analysis above, by fitting the high-temperature part of the data with a straight line $r(T) = aT + b$. Since in both MAT4G and MAT5G the slope of the linear-in-temperature component (a) is fairly small (Fig. 2g,h), in many cases $r(T)$ can simply be replaced by a constant resistance value measured above T_c, and this method was used for device 4C shown in Extended Data Fig. 8e. For a given percentage p, we found the intersection of the zero-field resistance curve with $p \times r(T)$, which defines resistance R_N^p and temperature $T_c^p(0)$. We used R_N^p to define the resistance contours in Fig. 3e–g and fit each contour to $T = T_c^p(0)(1 - \alpha_p B_\parallel^2)$ from $T_c^p(0)$ down to lowest temperature we could measure, where α_p is a fitting parameter. The zero-temperature critical field was obtained through extrapolation, $B_c^p(0) = \alpha_p^{-1/2}$. The corresponding PVR is then $\mathrm{PVR}^p = B_c^p(0)/[1.86\,\mathrm{T\,K^{-1}}\,T_c^p(0)]$. This procedure was independently performed for each ν and p = 10%, 20%, 30%. We found that the choice of the threshold percentage makes no qualitative difference in the extracted PVR.

Band structure and orbital g-factor in MATNG. We calculated the band structures using the continuum model that is extended from twisted bilayer graphene[28,29]. The Hamiltonian of the system can be formally written as

$$H_0(\mathbf{k}) = \begin{bmatrix} \hbar v_F \boldsymbol{\sigma}^{\theta/2} \cdot \mathbf{k} & T & 0 & \cdots & 0 \\ T^\dagger & \hbar v_F \boldsymbol{\sigma}^{-\theta/2} \cdot \mathbf{k} & T^\dagger & \cdots & 0 \\ 0 & T & \hbar v_F \boldsymbol{\sigma}^{\theta/2} \cdot \mathbf{k} & \cdots & 0 \\ \vdots & \vdots & \vdots & \ddots & \vdots \\ 0 & 0 & 0 & \cdots & \hbar v_F \boldsymbol{\sigma}^{\pm\theta/2} \cdot \mathbf{k} \end{bmatrix},$$

where $\sigma^{\pm\theta/2}$ are Pauli matrices that are rotated by angles $\pm\theta/2$, T is an interlayer coupling matrix identical to that in twisted bilayer graphene, v_F is the Fermi velocity in monolayer graphene and $\hbar$ is the reduced Planck constant. Each row/column here represents one layer in the system. The sign in the last element of the matrix is determined by whether N is odd (+) or even (−). For simplicity, only direct tunnelling between adjacent layers is considered. We numerically diagonalized this Hamiltonian for different wave vectors $\mathbf{k}$ in the mini Brillouin zone of the superlattice corresponding to twist angle θ and obtained the energy dispersions, which are plotted in Fig. 1d–g for $N = 2, 3, 4, 5$ near their magic angles, respectively. The spectrum was calculated and plotted for the K valley only. The spectrum of the K′ valley is related to the K spectrum by time-reversal symmetry, and thus can by obtained simply by taking $\mathbf{k} \to -\mathbf{k}$. The parameters we used are AB site hopping amplitude $w = 0.1$ eV and AA site hopping amplitude $w' = 0.08$ eV.

To include the effect of an in-plane magnetic field $\mathbf{B} = B\hat{n}$, where $\hat{n}$ is the direction of the field and satisfies $\hat{n} \cdot \hat{z} = 0$ ($\hat{z}$ is unit vector along the perpendicular direction), we can pick the gauge $\mathbf{A} = zB\hat{n} \times \hat{z}$, such that $\nabla \times \mathbf{A} = \mathbf{B}$. Through minimal coupling substitution $\mathbf{k} \to \mathbf{k} + \frac{e}{\hbar}\mathbf{A}$ and defining $\hat{t} = \hat{n} \times \hat{z}$, one can write the Hamiltonian in the field as

$$H(\mathbf{k}, B) = \begin{bmatrix} \hbar v_F \boldsymbol{\sigma}^{\theta/2} \cdot (\mathbf{k} + \frac{N-1}{2} edB\hat{t}/\hbar) & T & 0 & \cdots & 0 \\ T^\dagger & \hbar v_F \boldsymbol{\sigma}^{-\theta/2} \cdot (\mathbf{k} + \frac{N-3}{2} edB\hat{t}/\hbar) & T^\dagger & \cdots & 0 \\ 0 & T & \hbar v_F \boldsymbol{\sigma}^{\theta/2} \cdot (\mathbf{k} + \frac{N-5}{2} edB\hat{t}/\hbar) & \cdots & 0 \\ \vdots & \vdots & \vdots & \ddots & \vdots \\ 0 & 0 & 0 & \cdots & \hbar v_F \boldsymbol{\sigma}^{\pm\theta/2} \cdot (\mathbf{k} - \frac{N-1}{2} edB\hat{t}/\hbar) \end{bmatrix},$$

where d is the interlayer distance. Conceptually, the application of an in-plane B corresponds to shifting the Dirac cones in each layer before hybridizing them, by an amount $\Delta\mathbf{k} = edB\hat{t}/\hbar$ between adjacent layers. This is commonly called a 'momentum boost'. Since the time-reversal symmetry is now broken, the K′ valley spectrum needs to be obtained separately by replacing all $\mathbf{k}$ with $-\mathbf{k}$ in the Hamiltonian above.

To obtain the orbital g-factor g_{orb}, we obtained the spectrum in both K and K′ valleys and calculated $|E_K(\mathbf{k}, B) - E_{K'}(-\mathbf{k}, B)|$, averaged over the entire Brillouin zone and as a function of B. We call this quantity $\overline{\Delta E}(B)$. In all of these calculations, we set the direction of the field to be along the x axis for simplicity. $\overline{\Delta E}(B)$ characterizes the magnitude of the orbital depairing effect assuming that the superconducting Cooper pairs are formed by electrons with momentum $\mathbf{k}$ in the K valley and $-\mathbf{k}$ in the K′ valley, that is an intervalley pairing. We obtained an average g_{orb} from its leading order dependence on B: $\overline{\Delta E}(B) = g_{orb}\mu_B B + O(B^2)$. The Brillouin zone averaging was carried out only in the flat bands in each MATNG system, and the resulting g_{orb} is plotted in Fig. 4b.

Without displacement field, this calculation shows that all MATNG with odd N have zero g_{orb} and those with even N have g_{orb} that quickly decays with increasing N.

We can understand this effect from a simple perturbation theory argument. If we write the above Hamiltonian as $H(\mathbf{k}, B) = H_0(\mathbf{k}) + BH'(\mathbf{k})$, where

$$H'(\mathbf{k}) = \tfrac{v_F ed}{2} \begin{bmatrix} (N-1)\boldsymbol{\sigma}^{\theta/2}\cdot\hat{t} & 0 & 0 & \dots & 0 \\ 0 & (N-3)\boldsymbol{\sigma}^{-\theta/2}\cdot\hat{t} & 0 & \dots & 0 \\ 0 & 0 & (N-5)\boldsymbol{\sigma}^{\theta/2}\cdot\hat{t} & \dots & 0 \\ \vdots & \vdots & \vdots & \ddots & \vdots \\ 0 & 0 & 0 & \dots & -(N-1)\boldsymbol{\sigma}^{\pm\theta/2}\cdot\hat{t} \end{bmatrix}.$$

First-order perturbation theory predicts an energy shift

$$\Delta E = E(\mathbf{k}, B) - E(\mathbf{k}, 0) = B\langle\psi_0(\mathbf{k})| H'(\mathbf{k}) |\psi_0(\mathbf{k})\rangle,$$

where $|\psi_0(\mathbf{k})\rangle$ is an eigenstate of $H_0(\mathbf{k})$. To evaluate this expression for the flat bands at its largest magic angle and taking the chiral limit assumption (setting w' to zero), we quote an expression from ref. [37],

$$|\psi_0(\mathbf{k})\rangle = \begin{bmatrix} |\psi_1\rangle \\ |\psi_2\rangle \\ \vdots \\ |\psi_N\rangle \end{bmatrix}, \begin{cases} |\psi_{2m}\rangle &= \sqrt{\tfrac{4}{N+1}}\sin\left(\tfrac{2m\pi}{N+1}\right)\left|\psi_2^{\mathrm{MATBG}}\right\rangle \\ |\psi_{2m+1}\rangle &= \sqrt{\tfrac{4}{N+1}}\sin\left(\tfrac{(2m+1)\pi}{N+1}\right)\left|\psi_1^{\mathrm{MATBG}}\right\rangle \end{cases}$$

where $\left|\psi_{1,2}^{\mathrm{MATBG}}\right\rangle$ constitutes a corresponding eigenstate of MATBG due to the mapping between the flat bands in MATNG and MATBG, and m is an integer. We chose to normalize all $|\psi_0(\mathbf{k})\rangle$ to one. Using this mapping relationship, we can reduce equation (4) to

$$\Delta E = \tfrac{v_F edB}{2}\left[\sum_{0<l\le N\,\mathrm{even}} 4\tfrac{N+1-2l}{N+1}\sin^2\left(\tfrac{l\pi}{N+1}\right)\left\langle\psi_2^{\mathrm{MATBG}}\right|\boldsymbol{\sigma}^{\theta/2}\cdot\hat{t}\left|\psi_2^{\mathrm{MATBG}}\right\rangle + \sum_{0<l\le N\,\mathrm{odd}} 4\tfrac{N+1-2l}{N+1}\sin^2\left(\tfrac{l\pi}{N+1}\right)\left\langle\psi_1^{\mathrm{MATBG}}\right|\boldsymbol{\sigma}^{-\theta/2}\cdot\hat{t}\left|\psi_1^{\mathrm{MATBG}}\right\rangle\right].$$

If we denote

$$\epsilon_1 = \frac{v_F ed}{2}\left\langle\psi_1^{\mathrm{MATBG}}\right|\boldsymbol{\sigma}^{\theta/2}\cdot\hat{t}\left|\psi_1^{\mathrm{MATBG}}\right\rangle,$$

$$\epsilon_2 = \frac{v_F ed}{2}\left\langle\psi_2^{\mathrm{MATBG}}\right|\boldsymbol{\sigma}^{-\theta/2}\cdot\hat{t}\left|\psi_2^{\mathrm{MATBG}}\right\rangle,$$

which are quantities weakly dependent on N, then we can further write

$$\Delta E = \sum_{0<l\le N\,\mathrm{odd}} 4\tfrac{N+1-2l}{N+1}\sin^2\left(\tfrac{l\pi}{N+1}\right)B\epsilon_1 + \sum_{0<l\le N\,\mathrm{even}} 4\tfrac{N+1-2l}{N+1}\sin^2\left(\tfrac{l\pi}{N+1}\right)B\epsilon_2$$

If N is odd, noting that $\sin\left(\tfrac{l\pi}{N+1}\right) = \sin\left(\tfrac{(N+1-l)\pi}{N+1}\right)$,

$$\Delta E = 4B\epsilon_1\left[-(N-1)\sin^2\left(\tfrac{\pi}{N+1}\right) + \dots + (N-1)\sin^2\left(\tfrac{N\pi}{N+1}\right)\right]/(N+1)$$

$$+4B\epsilon_2\left[-(N-3)\sin^2\left(\tfrac{2\pi}{N+1}\right) + \dots + (N-3)\sin^2\left(\tfrac{(N-1)\pi}{N+1}\right)\right]/(N+1)$$

$$= 0.$$

This result can be obtained from an argument based on mirror symmetry as well[45,48].

If N is even,

$$\Delta E = 4B\epsilon_1\left[-(N-3)\sin^2\left(\tfrac{2\pi}{N+1}\right) + \dots + (N-1)\sin^2\left(\tfrac{N\pi}{N+1}\right)\right]/(N+1)$$

$$+4B\epsilon_2\left[-(N-1)\sin^2\left(\tfrac{\pi}{N+1}\right) + \dots + (N-3)\sin^2\left(\tfrac{(N-1)\pi}{N+1}\right)\right]/(N+1)$$

$$= \frac{4B(\epsilon_1-\epsilon_2)}{N+1}\sum_{j=1}^{N/2}(N+1-2j)(-1)^{j-1}\sin^2\left(\frac{j\pi}{N+1}\right)$$

$$= \frac{1}{N+1}\left[1 - \frac{\cos\left(\tfrac{2\pi}{N+1}\right)}{\cos^2\left(\tfrac{\pi}{N+1}\right)}\right]\cdot B(\epsilon_1-\epsilon_2)$$

As N increases, the prefactor approaches zero rapidly and asymptotically behaves as $\sim\pi^2(N+1)^{-3}$ when N is large. When $N=2$, the prefactor evaluates to one and ΔE is the largest. As we increase to $N=4, 6, 8, \dots$, it becomes 0.106, 0.033, 0.015, respectively. These estimations qualitatively explain why all $N>2$ MATNG systems exhibit much smaller in-plane orbital effect and g_{orb} than MATBG, regardless of whether N is even or odd.

Inhomogeneous gating across layers in multilayer graphene systems. Typically, electrostatic gating in atomically thin materials is considered to be geometric, that is the charge density and electric displacement field within the material are assumed to be simply related to top and bottom gate voltages V_{tg} and V_{bg} by

$$n = \frac{1}{e}\left(c_{\mathrm{tg}}V_{\mathrm{tg}} + c_{\mathrm{bg}}V_{\mathrm{bg}}\right),$$

$$D = \frac{1}{2}\left(-c_{\mathrm{tg}}V_{\mathrm{tg}} + c_{\mathrm{bg}}V_{\mathrm{bg}}\right),$$

where c_{tg} and c_{bg} are capacitance per area of top and bottom dielectrics, respectively. Since the material is thin, the charge density and displacement field can be assumed to be uniform across the thickness. However, as more layers are added, electrostatic screening by the outer layers becomes non-negligible and creates a non-uniform distribution of charge density and displacement field among the graphene layers. This distribution will in turn alter the electronic dispersion of the system. Solving for both band dispersion and charge distribution simultaneously and self-consistently requires a Hartree–Fock type calculation for each V_{tg} and V_{bg}, which is a challenging computation task and beyond the scope of this work.

Instead, we included the zeroth order effect of such non-uniform screening into the continuum model by treating each graphene layer as a metal with constant density of states (DOS) $\mathcal{D} = \mathrm{d}n/\mathrm{d}\mu$ (μ is the chemical potential), and then considered the screening of the electric field by them. The screening effect was incorporated by modelling the graphene stack as a capacitor network, as illustrated in Extended Data Fig. 6b. Here $c_{\mathrm{g}} = \epsilon_0/d$ represents the geometric capacitance between the graphene layers, and $c_{\mathrm{q}} = e^2\mathcal{D}$ represents the quantum capacitance of each graphene layer (all discussions below assume unit area). The voltage across c_{q} equals $-\mu/e$, and the charge stored on c_{q}, which equals $\int_0^{-\mu/e} c_{\mathrm{q}}\mathrm{d}v_{\mathrm{q}} = -e\int_0^{\mu}\mathcal{D}\mathrm{d}\mu = -en$, is exactly the charge density on the graphene layer. The voltage on the left node of each c_{q}, which we denote v_i, represents the electrostatic potential of the ith graphene layer, while the voltage on the right node, which equals $-\mu_{ei}/e$, is zero because they are grounded. μ_{ei} is the electrochemical potential of the ith layer and by definition $\mu_{ei} = \mu_i - ev_i$. This relationship is guaranteed by the Kirchhoff voltage law in the circuit formulation.

The solution of this capacitor network $\mathbf{v}^T = \begin{bmatrix} v_1 v_2 \dots v_N \end{bmatrix}^T$ satisfies

$$\begin{bmatrix} c_{\mathrm{q}}+c_{\mathrm{g}}+c_{\mathrm{tg}} & -c_{\mathrm{g}} & 0 & \dots & 0 \\ -c_{\mathrm{g}} & c_{\mathrm{q}}+2c_{\mathrm{g}} & -c_{\mathrm{g}} & \dots & 0 \\ 0 & -c_{\mathrm{g}} & c_{\mathrm{q}}+2c_{\mathrm{g}} & \dots & 0 \\ \vdots & \vdots & \vdots & \ddots & \vdots \\ 0 & 0 & 0 & \dots & c_{\mathrm{q}}+c_{\mathrm{g}}+c_{\mathrm{bg}} \end{bmatrix}\mathbf{v} = \begin{bmatrix} c_{\mathrm{tg}}v_{\mathrm{tg}} \\ 0 \\ 0 \\ \vdots \\ c_{\mathrm{bg}}v_{\mathrm{bg}} \end{bmatrix}.$$

Since typically $c_{\mathrm{tg}}, c_{\mathrm{bg}} \ll c_{\mathrm{q}}, c_{\mathrm{g}}$, they can be dropped from the left side of the matrix. We can thus write

$$\begin{bmatrix} c_{\mathrm{q}}+c_{\mathrm{g}} & -c_{\mathrm{g}} & 0 & \dots & 0 \\ -c_{\mathrm{g}} & c_{\mathrm{q}}+2c_{\mathrm{g}} & -c_{\mathrm{g}} & \dots & 0 \\ 0 & -c_{\mathrm{g}} & c_{\mathrm{q}}+2c_{\mathrm{g}} & \dots & 0 \\ \vdots & \vdots & \vdots & \ddots & \vdots \\ 0 & 0 & 0 & \dots & c_{\mathrm{q}}+c_{\mathrm{g}} \end{bmatrix}\mathbf{v} = \begin{bmatrix} -en_{\mathrm{tg}} \\ 0 \\ 0 \\ \vdots \\ -en_{\mathrm{bg}} \end{bmatrix},$$

where n_{tg} and n_{bg} are the electron density induced by the top and bottom gates, respectively.

To consider an external displacement field from differential gating, we set $n_{\mathrm{tg}} = -n_{\mathrm{bg}} = D/e$ and solve equation (20) numerically to obtain the electrostatic potential on each layer v_i. Extended Data Figure 6c shows v_i solved for $N=2, \dots, 6$.

An energy $-ev_i$ was then added onto the corresponding diagonal terms in the continuum Hamiltonian, equation (1), to include the screened electrostatic effect into the continuum model. As an estimate of the mean density of states on each layer, we assumed $\mathcal{D} = n_s/(NW)$, where n_s is superlattice density and $W \sim 20$ meV is the approximate bandwidth for the flat bands (regardless of N). Examples of calculated MATNG band structures using the screened electrostatic potentials are shown in Extended Data Fig. 1 for $N = 2, 3, 4, 5$.

We note that while the continuum model can include the effect of non-uniform electrical displacement field as described above, it does not allow inclusion of information on the filling factor at the single-particle level. However, for large N MATNG structures, especially MAT5G, the inhomogeneous filling factor among layers could play an important role in its ν–D phase diagram, and may explain why superconductivity in MAT5G slightly extends beyond $\nu = 4$. We hope that future numerical studies which self-consistently include both of the above effects can elucidate the whole picture.

Fraunhofer-like oscillation pattern. To see a clear Fraunhofer-like pattern in MAT4G, we fabricated a device with split top gates with a nominal gap of 150 nm. A picture of the device is shown in Extended Data Fig. 7a (the relevant contacts are labelled as JJ) and schematically illustrated in Extended Data Fig. 7b. Since MAT4G under the gap region is not covered by the top gate, it can be doped into a normal state (N) while the dual-gated regions are doped into superconductivity (S), thereby forming a 'SNS' Josephson junction. We note that in these types of 2D Josephson junctions, the oscillation periodicity generally does not correspond to the junction area (that is defined by the gap between the split gates), as 2D superconductors do not exhibit the Meissner effect that expels all magnetic fields from the leads of the junction. This was previously observed in Josephson junctions made from MATBG[40] and has a solid theoretical background (see, for example, ref. [49]). In these junctions, the Fraunhofer oscillation period is determined by the width of the entire device w, approximately equalling $\sim 1.8\phi_0/w^2$, where $\phi_0 = h/2e$ is the flux quantum. Taking $w \sim 2\,\mu$m, the period should be about 1 mT, which is qualitatively consistent with the visible modulations in Fig. 2c.

Discussion about other possible effects. In our understanding, the superconductivity across the magic family originates from a common but as yet undetermined mechanism, and the interaction effects in their respective flat bands are similar (for example, spontaneous flavour symmetry breaking at $D = 0$). Some of the apparent differences among the family can be at least partially attributed to one of three factors: (1) increasing magic angle with the number of layer N, (2) more Dirac-like/dispersive TBG-like bands coexisting with the flat bands as N increases and (3) different strengths of orbital coupling due to the mirror symmetry, as discussed in Fig. 4 in the main text. Since all structures are prepared on the same substrate (hBN), we do not expect the substrate to be a varying factor in these comparisons. Having larger magic angles and thus smaller moiré unit cells, the four-layer and five-layer structures should be less susceptible to strain and relaxation effects. However, having more interfaces also implies that there are more possible modes of twist angle disorder. Further studies are necessary to elucidate the roles of these effects.

In typical bulk superconductors, the pair-breaking effect is usually modelled by the Werthamer–Helfand–Hohenberg theory. We note, however, that this theory does not directly work for 2D superconductors in an in-plane magnetic field as there are no vortices. The observation of re-entrant superconducting states in MATTG and hints of these in MAT4G and MAT5G introduce further complications. We invite future works to develop a robust method to analyse these effects more quantitatively.

The resistive features at integer ν are generally robust, especially in relatively less disordered devices (defined by cleaner Landau levels). On the other hand, resistive states at fractional values appear to be dependent on the sample, possibly due to their different angles. One possible origin of these fractional features is the formation of charge density waves, which was identified in the recent scanning SET experiments on MATBG[35].

Data availability

The data that support the current study are available from Harvard Dataverse[50].

Code availability

The codes that support the current study are available from Harvard Dataverse[50].

References

49. Moshe, M., Kogan, V. G. & Mints, R. G. Edge-type Josephson junctions in narrow thin-film strips. *Phys. Rev. B* **78**, 020510 (2008).
50. Park, J. et al. Data for robust superconductivity in magic-angle multilayer graphene family. *Harvard Dataverse* https://doi.org/10.7910/DVN/XZV9ON (2022).

Acknowledgements

We thank A. Vishwanath, E. Khalaf and P. Ledwith for fruitful discussions. This work was primarily supported by the US Department of Energy (DOE), Office of Basic Energy Sciences (BES), Division of Materials Sciences and Engineering under award DE-SC0001819 (J.M.P. and S.S.). Help with transport measurements and data analysis were supported by the National Science Foundation (DMR-1809802), and the STC Center for Integrated Quantum Materials (NSF grant no. DMR-1231319) (Y.C.). Help with device fabrication was supported by the Air Force Office of Scientific Research (AFOSR) 2DMAGIC MURI FA9550-19-1-0390 (L.X.). P.J.-H. acknowledges support from the Gordon and Betty Moore Foundation's EPiQS Initiative through grant no. GBMF9463. P.J.-H. acknowledges partial support by the Fundación Ramon Areces and the CIFAR Quantum Materials programme. The development of new nanofabrication and characterization techniques enabling this work was supported by the US DOE Office of Science, BES, under award DE-SC0019300. K.W. and T.T. acknowledge support from the Elemental Strategy Initiative conducted by MEXT, Japan (grant no. JPMXP0112101001), JSPS KAKENHI (grant no. JP20H00354), CREST(grant no. JPMJCR15F3) and JST. This work made use of the Materials Research Science and Engineering Center Shared Experimental Facilities supported by the National Science Foundation (grant no. DMR-0819762) and of Harvard's Center for Nanoscale Systems, supported by the NSF (grant no. ECS-0335765).

Author contributions

J.M.P. and Y.C. fabricated the samples and performed transport measurements, with help from L.-Q.X. and S.S. K.W. and T.T. provided hBN samples. J.M.P. and Y.C. performed numerical simulations. J.M.P., Y.C. and P.J.-H. performed data analysis, discussed the results and wrote the manuscript with input from all co-authors.

Competing interests

The authors declare no competing interests.

Additional information

Extended data is available for this paper at https://doi.org/10.1038/s41563-022-01287-1.

Correspondence and requests for materials should be addressed to Jeong Min Park or Pablo Jarillo-Herrero.

Peer review information *Nature Materials* thanks Chun Ning Lau, Aaron Sharpe and the other, anonymous, reviewer(s) for their contribution to the peer review.

Reprints and permissions information is available at www.nature.com/reprints.

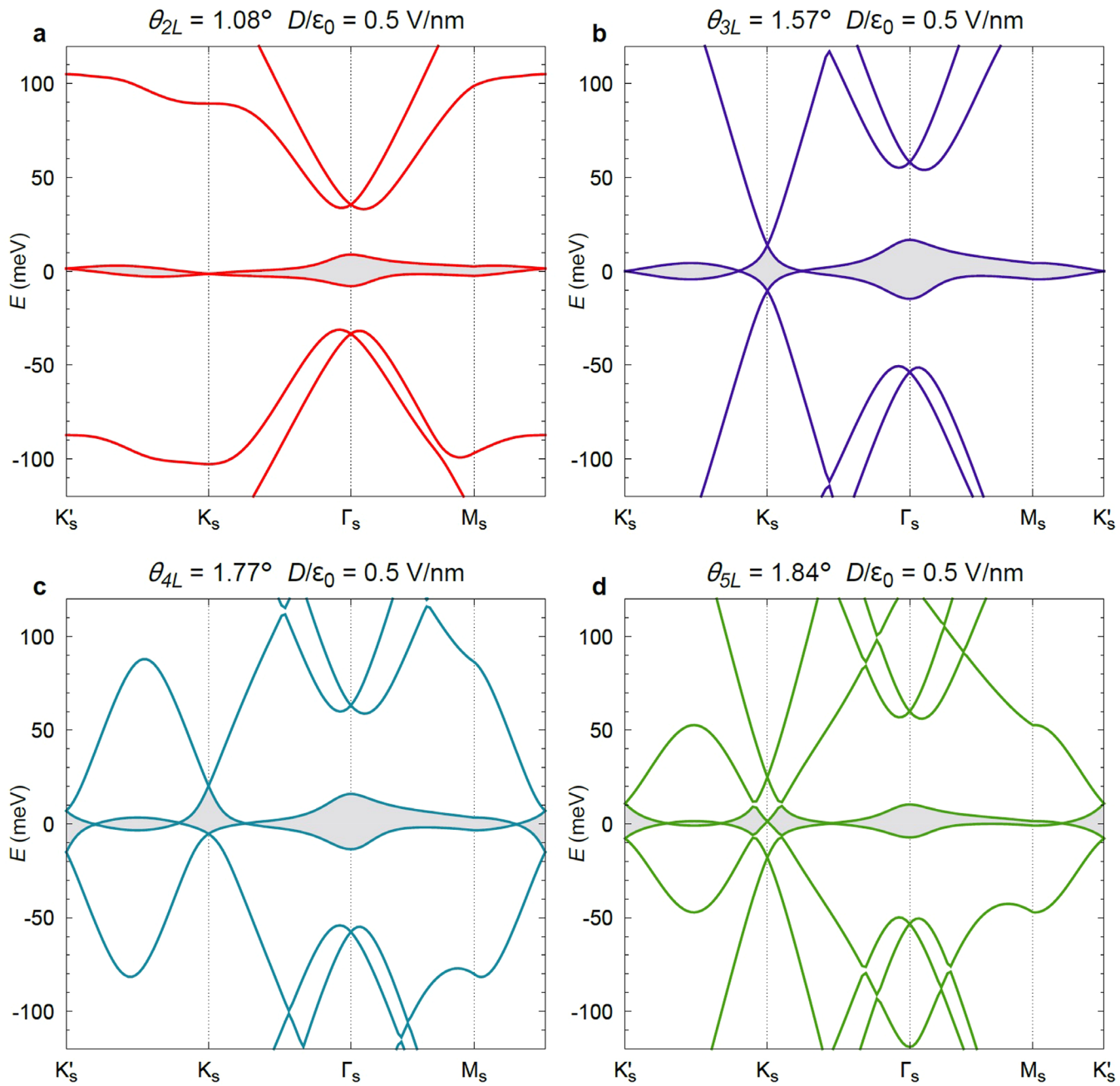

Extended Data Fig. 1 | Calculated band structure of MATNG in the presence of electric displacement field $\frac{D}{\varepsilon_0} = 0.5$ V/nm. The calculation uses the screened electrostatic potential calculated as illustrated in Extended Data Fig. 6c. For all N>2 MATNG structures, the electric displacement field hybridizes the flat bands with other dispersive bands.

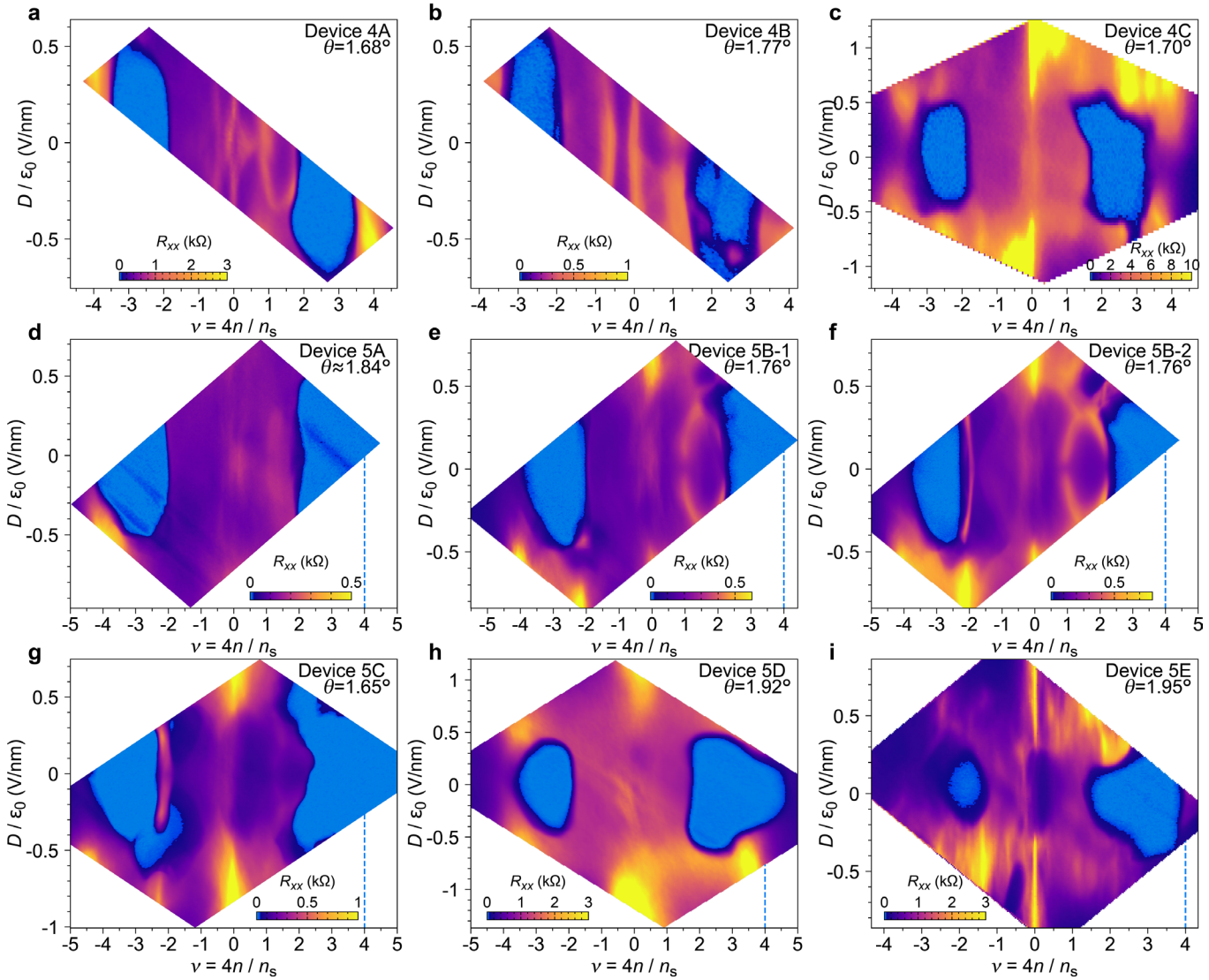

Extended Data Fig. 2 | ν-D phase diagrams of MAT4G and MAT5G devices. Devices 4A-C shown in (a-c) are MAT4G devices, while Devices 5A-E shown in (d-i) are MAT5G devices. Device 5B-1 and 5B-2 are two different contacts from the same device that shares the same top gate and back gate. All measurements were performed at T ~ 200 mK. In all MAT5G devices, we find the superconductivity region to be either approaching or exceeding $\nu = 4$, which is indicated by blue dashed lines in (d-i).

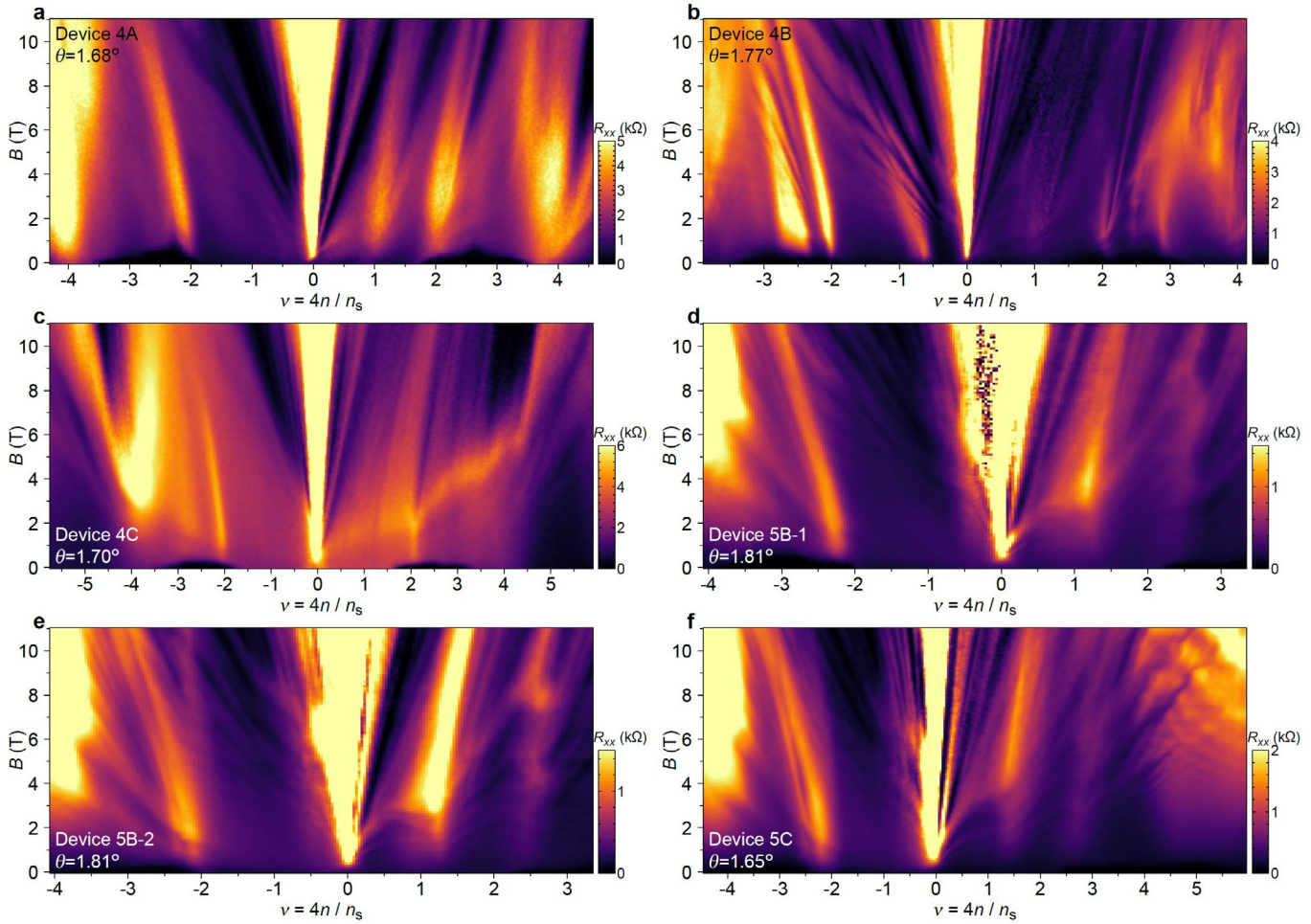

Extended Data Fig. 3 | Landau fan diagrams of MAT4G and MAT5G devices. All measurements were performed at T ~ 200 mK.

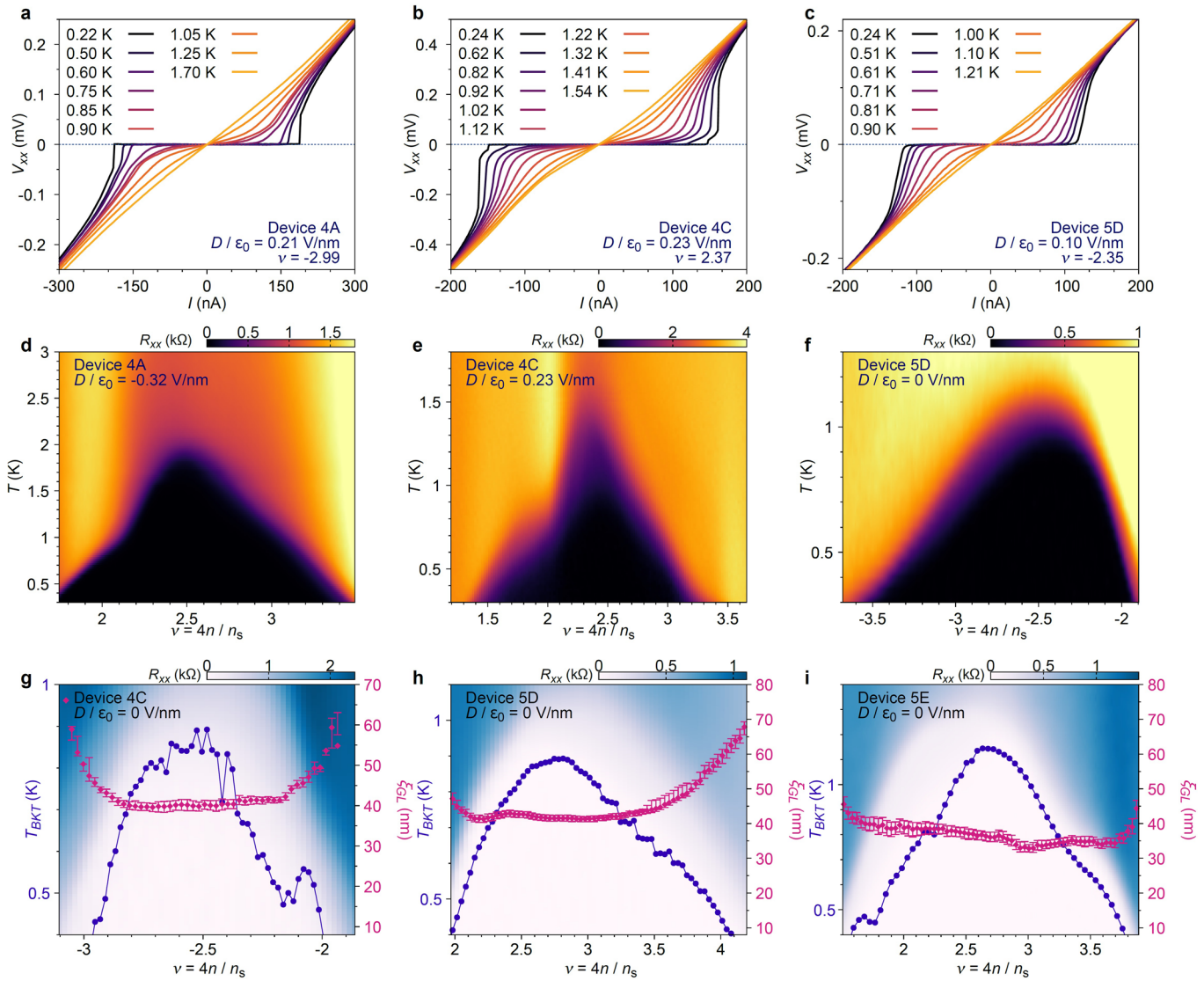

Extended Data Fig. 4 | Superconducting properties in other MAT4G and MAT5G devices. (a-c) Temperature-dependent $V_{xx} - I$ curves in device 4A, 4C and 5D. (d-f) $\nu - T$ phase diagrams in device 4A, 4C and 5D. (g-i) T_{BKT} and Ginzburg-Landau coherent length ξ_{GL} in device 4C, 5D and 5E. The error bars in (g-i) correspond to ξ_{GL} extracted using p=30% (point), 35% (lower bound), and 25% (upper bound).

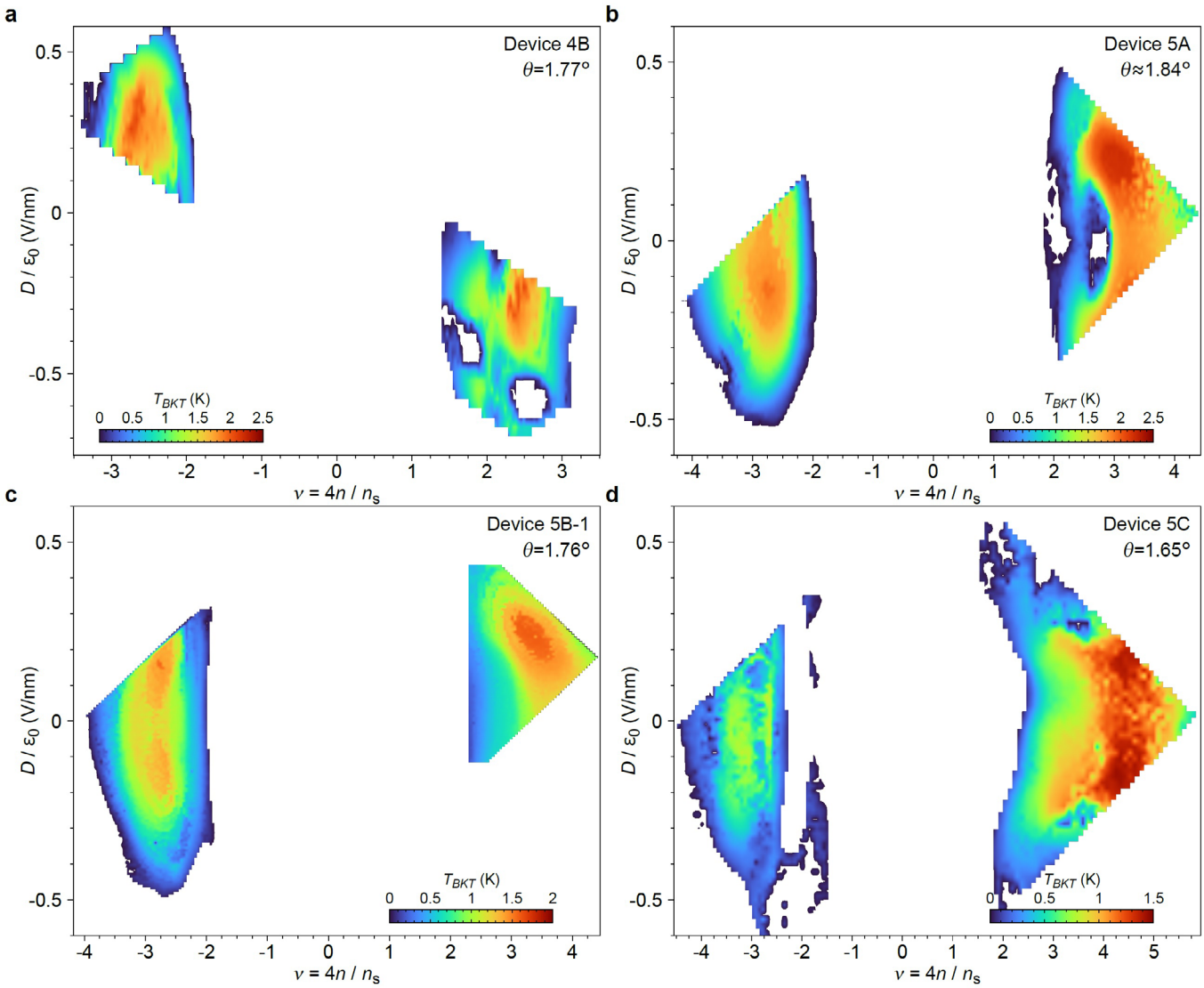

Extended Data Fig. 5 | ν-D map of BKT transition temperature in device 4B, 5A, 5B-1, and 5C. (a-d) T_{BKT} as a function of ν and D in device 4B (a), 5A (b), 5B-1 (c), and 5C (d).

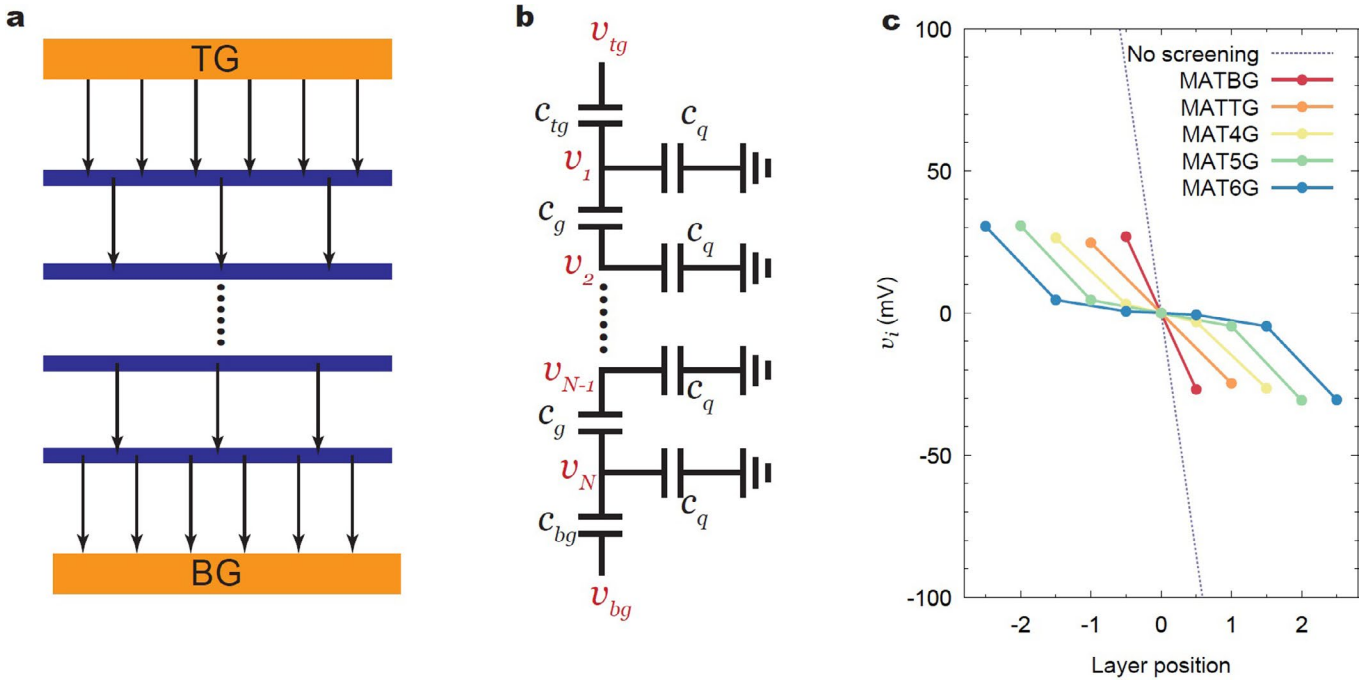

Extended Data Fig. 6 | Modeling layer-inhomogeneous screening in MATNG. (a) Schematic of N graphene layers being gated by a top gate (TG) and bottom gate (BG). The electric displacement field between the graphene layers is reduced compared to the field outside the stack due to screening. (b) By assuming a finite density of states $\mathcal{D}$ on each graphene layer, we model the N-layer system as a capacitor network, where $c_q = e^2\mathcal{D}$ is the quantum capacitance and $c_g = \varepsilon_0/d$ is the geometric capacitance. (c) Calculated electrostatic potential v_i on each layer for MATBG, MATTG, MAT4G, MAT5G and MAT6G (N = 2, …, 6), assuming bandwidth W=20 meV, and external displacement field $\frac{D}{\varepsilon_0} = 0.5V/nm$. The twist angle is the same as in Fig. 4, except for 6L which is 1.99°. Here the midplane (the plane of the $\frac{N+1}{2}$-th layer when N is odd and the midplane between $\frac{N}{2}$-th layer and $(\frac{N}{2}+1)$-th layer when N is even) is set to be zero both in layer position and in electrostatic potential. For comparison, the electrostatic potential without screening $eDdx/\varepsilon_0$ is shown as the dashed line, where $-\frac{(N-1)}{2} < x < \frac{(N-1)}{2}$ is the layer position (horizontal axis) and d=0.34 nm is the interlayer distance).

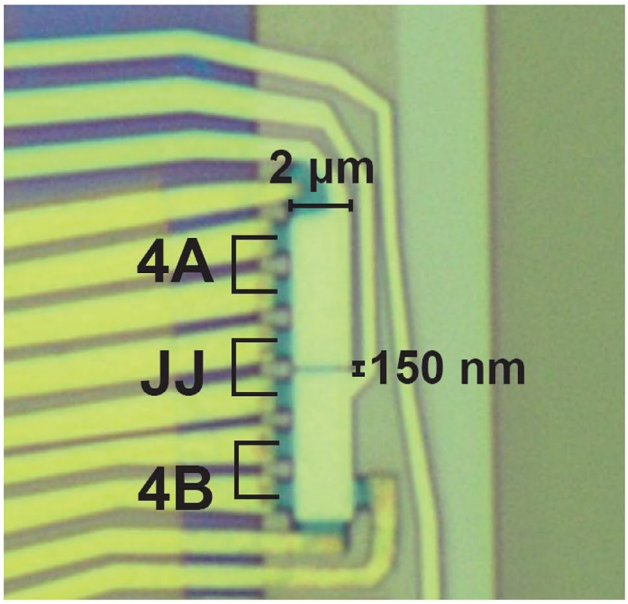

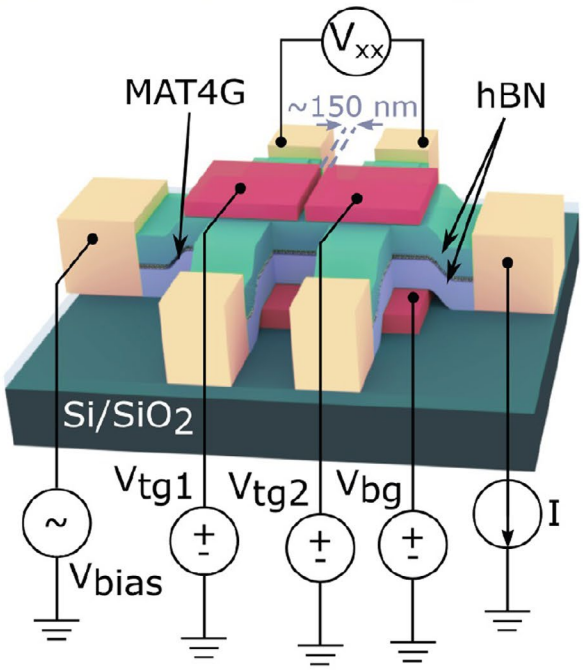

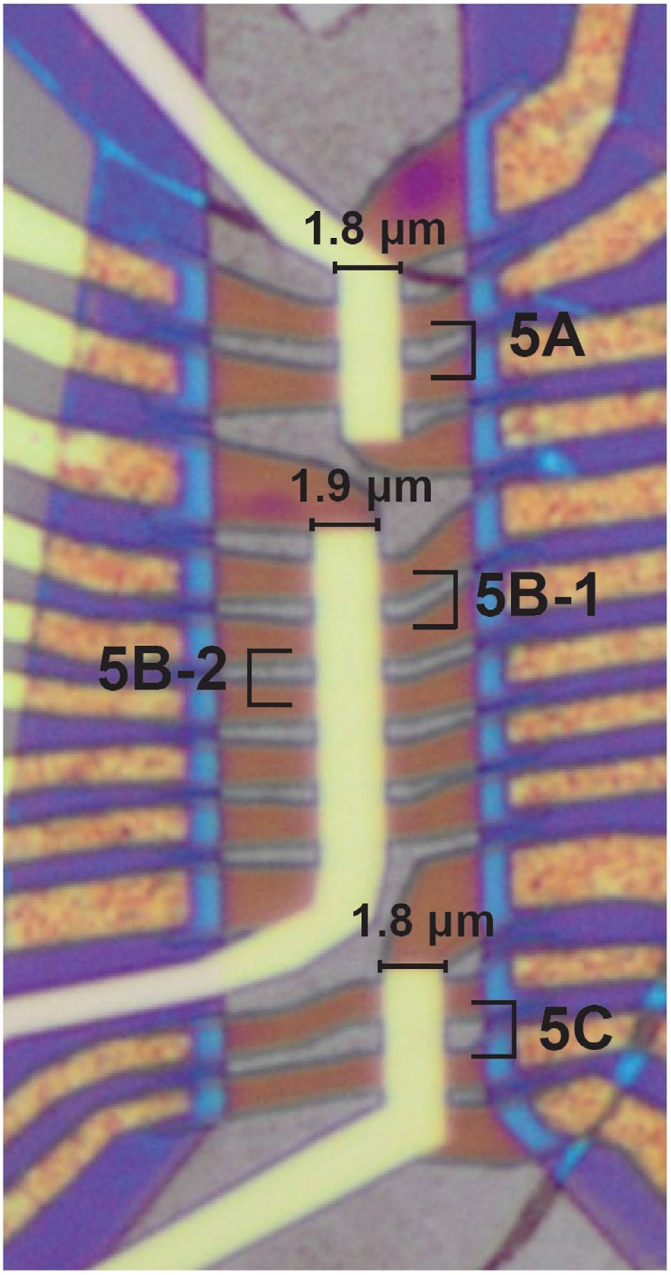

Extended Data Fig. 7 | Typical optical microscope images for MAT4G and MAT5G devices. The illustration shows the split-gate geometry for the Josephson junction. Data from all contacts including the ones not shown in the figures exhibit robust superconductivity.

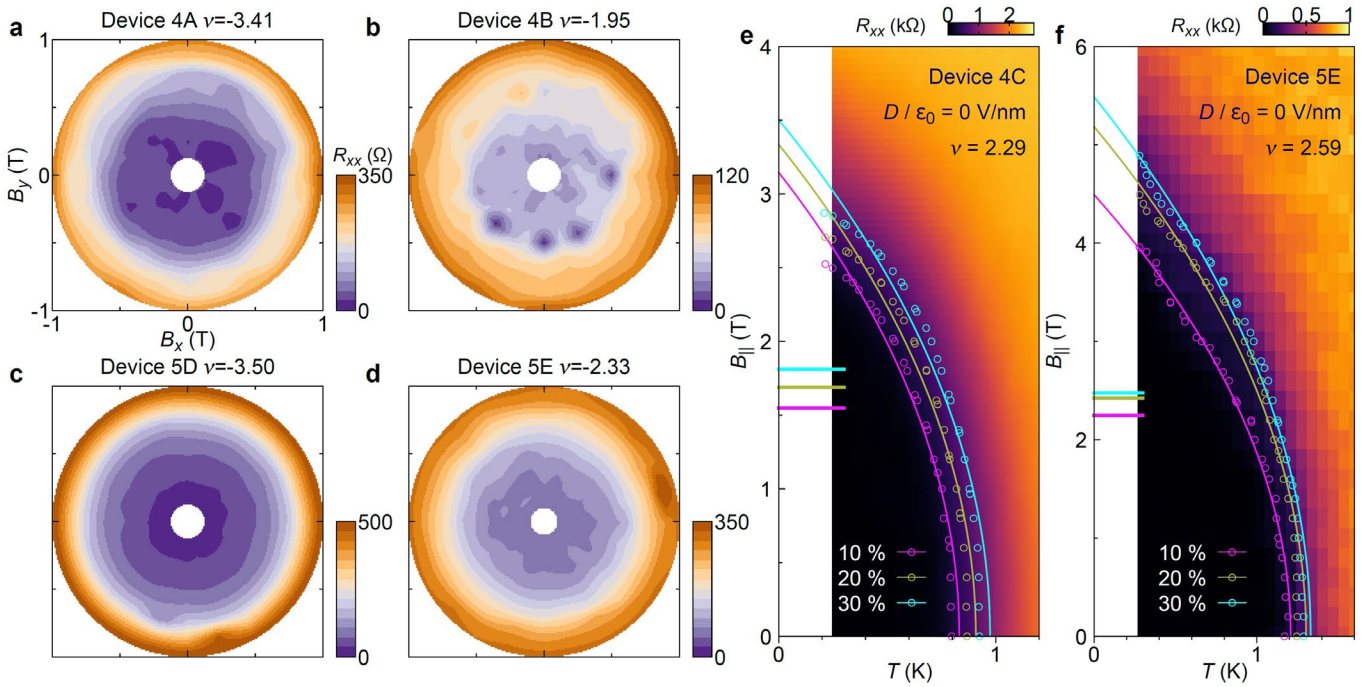

Extended Data Fig. 8 | In-plane magnetic field response in other MAT4G and MAT5G devices. (a-d) Absence of rotational symmetry breaking in other MAT4G and MAT5G devices. The filling factors for (a-d) are $\nu = -3.41, -1.95, -3.50, -2.33$, respectively, and the electric displacement fields are $\frac{D}{\varepsilon_0} = 0.29 V/nm, 0.29 V/nm, 0 V/nm, 0 V/nm$, respectively. (d-e) Pauli limit violation in Device 4C measured at $\nu = 2.29$ and $\frac{D}{\varepsilon_0} = 0 V/nm$ (d) and Device 5E measured at $\nu = 2.59$ and $\frac{D}{\varepsilon_0} = 0 V/nm$ (e).

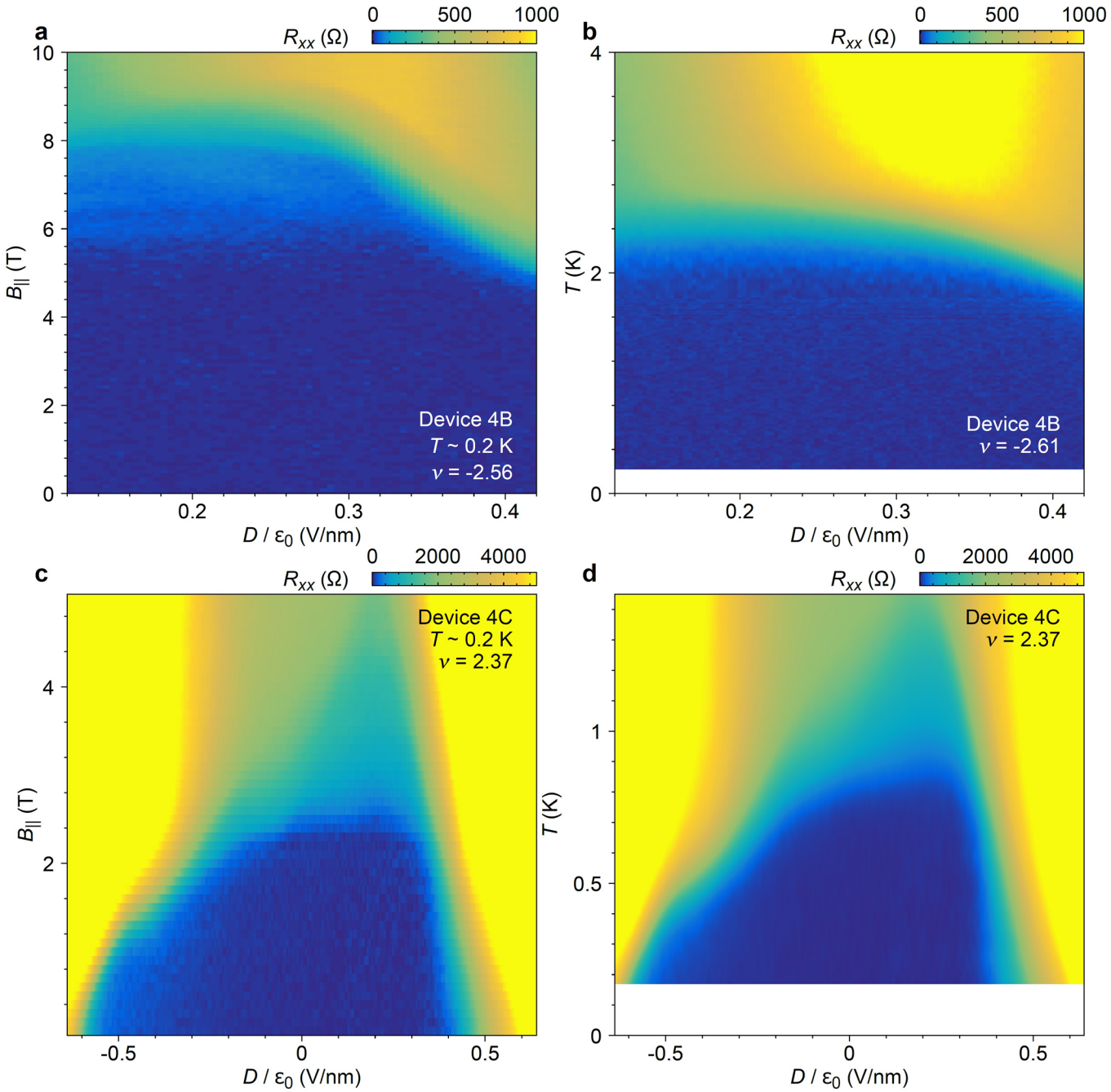

Extended Data Fig. 9 | D-independent Pauli limit violation in MAT4G. (a-b) shows the D-$B_{||}$and D-T map of R_{xx} in device 4B. We find the critical in-plane field and critical temperature follow similar trend with D, indicating that the PVR, which is proportional to the ratio between them, is largely independent of D. (c-d) Same trend is observed in device 4C.